International Journal of Coal Geology 269 (2023) 104219

Contents lists available at ScienceDirect

International Journal of Coal Geology

journal homepage: www.elsevier.com/locate/coal

The effects of Jurassic igneous intrusions on the generation and retention of gas shale in the Lower Permian source-reservoir shales of Karoo Basin, South Africa

Kenneth Chukwuma [a,*], Harilaos Tsikos [b], Brian Horsfield [c], Hans-Martin Schulz [c], Nicholas B. Harris [d], Madelaine Frazenburg [e]

[a] Department of Earth Science, University of Western Cape, 7535 Bellville, South Africa
[b] Department of Geology, University of Patras, 26504 Rio, Achaia, Greece
[c] GFZ German Research Centre for Geosciences, Telegrafenberg, 14473 Potsdam, Germany
[d] Department of Earth and Atmospheric Sciences, University of Alberta, Edmonton, AB T6G2E3, Canada
[e] Central Analytical Facilities, Department of Geology, Stellenbosch University, 7600, South Africa

ARTICLE INFO

Keywords:
Gas shale
Organic carbon
Igneous intrusions
Coke
Gas retention
Organic petrography
Intrusion-sediment interactions

ABSTRACT

Shale gas potential of the Whitehill Formation (Permian), Karoo Basin, South Africa is strongly influenced by widespread Jurassic igneous intrusions. A high-resolution organic petrographic and geochemical study is reported here on two stratigraphic sections, the objective being to gain insights into the chemical structure and alteration of oil-prone sedimentary organic matter during contact metamorphism. One section unaffected by intrusion served as background, while the other section was intruded by two laterally continuous dolerite sills with an average thickness of 10.7 and 9.3 m, preferentially emplaced at the upper and lower contacts of the formation, respectively. Heat flow from the sills caused TOC and S2 values from programmed pyrolysis to decline over a distance of 8.7 m from 3.2 to 0.15% and 4.65 to 0.11 mg HC/g TOC, respectively, and cause the reflectance of vitrinite and solid bitumen to increase from 2.03 to 5.82% and 1.58 to 7.87%.

Organic matter in the background samples is dominated by solid bitumen, a secondary thermal conversion product of oil-generative Type II kerogen. In the sill-hosting section, the thermal aureoles can be recognized by systematic changes to the optical texture and chemical structure and composition of solid bitumen. Solid bitumen particles develop anisotropy approaching the sills and become transformed into coke and pyrolytic carbon. $\delta^{13}C_{org}$ values become less negative by up to 3.13‰ VPDB. These data suggest significant devolatilization of organic matter to methane and destruction of petroleum generation and retention potential in the contact aureole of the sills. The trend of these datasets, coupled with the presence of several sills and their laterally extensive nature throughout much of the study area suggests that the intrusions have been significant in increasing methane generation on a basinal scale. Together, this study indicates that the complementary application of combined light and electron microscopy (CLEM), programmed pyrolysis, and isotope ratio mass spectrometry (IRMS) is suitable for a comprehensive characterization of organic matter alteration through the maturation continuum. Results also show that contact metamorphic alteration of organic matter by intrusions produced structural and compositional changes that are distinctive from those expected from geological burial maturation where graphite is the end-product.

1. Introduction

Organic maturation level is a fundamentally important consideration when evaluating the prospectivity of both conventional and unconventional petroleum systems (Tissot and Welte, 1984; Ross and Bustin, 2009; Mastalerz et al., 2018; Hackley et al., 2021; Liu et al., 2022). In shale-gas resource plays, where the quantity of gas in place depends on both the direct conversion of initial oil-prone organic matter to gas (primary cracking to gas) and secondary cracking of retained oil to gas, organic maturity determines the degree to which the total hydrocarbon

* Corresponding author.
E-mail addresses: chkken003@myuct.ac.za, 4177500@myuwc.ac.za (K. Chukwuma).

https://doi.org/10.1016/j.coal.2023.104219
Received 3 February 2023; Received in revised form 28 February 2023; Accepted 1 March 2023
Available online 5 March 2023

generation potential has been realized (Jarvie et al., 2007; Suárez-Ruiz et al., 2012; Mastalerz et al., 2018; Hackley et al., 2021; Teng et al., 2022). The development of nanoporosity within organic matter is also directly related to maturation (e.g., Loucks et al., 2012; Han et al., 2017; Dong and Harris, 2020; Teng et al., 2022). The organic nanopores are not only the main oil and gas storage sites in shales because of their large surface area and organic affinity but their high degree of connectivity also provides preferred migration pathways for the production of the stored hydrocarbon (e.g., Cardott et al., 2015; Mastalerz et al., 2018; Hackley et al., 2020; Liu et al., 2022). Thus, documenting the changes to quantity, structure, and chemical composition of organic matter in shales during maturation is of great significance for the evaluation of shales as oil and gas reservoirs.

The changes in the structure of dispersed organic macerals in shales with maturation remain poorly documented and understood, largely because of the inability of available tools to independently distinguish organic matter types petrographically (e.g., Katz and Arango, 2018; Mastalerz et al., 2018; Misch et al., 2019; Hackley et al., 2020, 2021; Liu et al., 2022). Current knowledge on the petrographic characterization of dispersed organic matter, including the structural and chemical changes

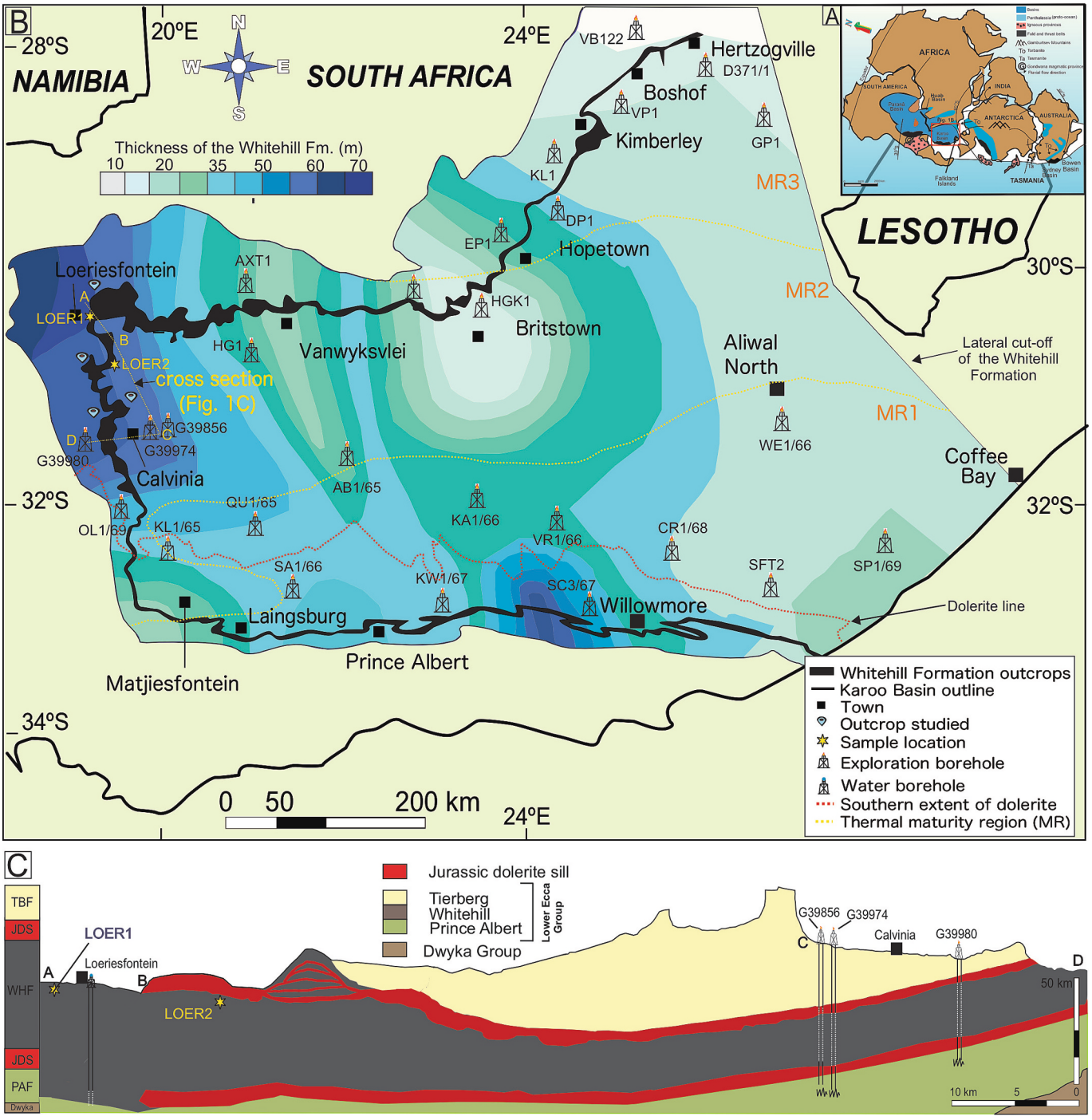

Fig. 1. A: Map of southwestern Gondwanan basins and their magmatic provinces and thrust belts during the Permian (modified from Faure and Cole, 1999). B: Map of southern Karoo Basin showing thermal maturity regions (MR; modified from Cole and McLachlan, 1991, 1994; de Kock et al., 2017), semi-continuous outcrop belt, and thickness distribution of the Whitehill Formation (after Chukwuma et al., 2018), boreholes, and the study location. C: Cross-section of the annotated points (A, B, C, D) in B, showing the geology of the study area and distribution of dolerite sills.

affecting oil-generative sedimentary organic matter during its conversion to oil and gas, has been most recently summarized by Hackley et al. (2021) and Liu et al. (2022). According to these studies, correlative microscopy (i.e., a combination of reflected-light and electron microscopy) offers an effective petrographic technique to distinguish organic matter types in shales (e.g., Mastalerz et al., 2018; Misch et al., 2019; Hackley et al., 2020). This promising method has been combined with laboratory-based cracking experiments to characterize organic matter alteration during maturation and to relate the changes to hydrocarbon generation, expulsion, and retention in shales (e.g., Vandenbroucke and Largeau, 2007; Bernard et al., 2012; Hackley et al., 2020, 2021; Teng et al., 2022).

The primary control on organic maturation is temperature, which typically results from increasing burial depth within sedimentary basins (e.g., Tissot and Welte, 1978; Radke et al., 1997). The accompanying formation of oil and gas is further controlled by non-isothermal reaction kinetics because temperature changes as a function of time under geological conditions (Espitalié et al., 1985; Yang and Horsfield, 2016). Temperature history depends on basin type and tectonic evolution with typical heating rates ranging between 0.5 and 5.0 K/My (e.g., Yang and Horsfield, 2016). However, the thermal evolution of some sedimentary basins is also dictated by igneous activity, including the intrusion of magmatic bodies, which are emplaced with much higher temperatures compared to their host rocks. Thus, igneous intrusions have profound effects on the temperature history of such basins, including the maturation of organic matter especially in the vicinity of the intrusions (e.g., Svensen et al., 2007; Wang and Manga, 2015; Mastalerz et al., 2018; Spacapan et al., 2018; Goodarzi et al., 2019; Rabbel et al., 2021). Heating rates up to twelve orders of magnitude higher have been reported where shales and coals have undergone maturation by contact metamorphism (e.g., Yang and Horsfield, 2016). Spacapan et al. (2018), and Goodarzi et al. (2019) have also shown that short-term but significantly higher intrusion-induced heating of oil-prone sedimentary organic matter produces structural and compositional characteristics that differ from those from burial-induced geological maturation.

Sedimentary basins in which igneous intrusions played a key role in thermal maturation include the Neuquén Basin (Argentina), Sverdrup Basin (Arctic Canada), Illinois Basin (USA), and Central Midland Valley (Scotland) (Svensen et al., 2007; Wang and Manga, 2015; Mastalerz et al., 2018; Goodarzi et al., 2019; Rabbel et al., 2021). The Karoo Basin of South Africa (Fig. 1) is another prime example and one where shale gas development is underway, as it may contain up to 390 trillion cubic feet (the equivalent of 11 trillion cubic meters) of resources (de Kock et al., 2017). Potential shale reservoirs were preferentially intruded by mid-Jurassic dolerite sills and dikes (Rowsell and De Swart, 1976; Svensen et al., 2007; Aarnes et al., 2011; de Kock et al., 2017). A wealth of work has evaluated the effect of these igneous intrusions in complicating the structural and thermal history of the basin and their implications for the Karoo shale hydrocarbon system (e.g., Aarnes et al., 2011; de Kock et al., 2017; Adeniyi et al., 2018; Nengovhela et al., 2021). These studies have mostly addressed the broad aspects of the impact of intrusions on the thermal and structural histories of the basin and are based largely on the mineralogical and associated chemical transformation of inorganic components. In terms of the organic matter, de Kock et al. (2017) described thermal devolatilization of the source rock reservoirs in the vicinity of dolerite sills using Rock-Eval/TOC (total organic carbon) data and desorbed gas volumes. However, the effect of the intrusions on the petrographic structure and chemical compositions of the organic matter and their implication for resource potential (gas content) of the basin is still a matter of debate.

The current study seeks to extend the knowledge of the effect of intrusions on the petrographic and geochemical evolution of oil-generative sedimentary organic matter in the principal gas shale reservoir unit in the basin, namely the Lower Permian Whitehill Formation. It aims to generate new insights into the thermal conversion of initial oil-prone sedimentary organic matter to petroleum, as well as migration and retention processes in response to heat flow from magmatic bodies. The outcomes are intended to inform new and refine existing predictive models of the impact of igneous intrusions on hydrocarbon generation and expulsion. The study is also designed to improve the methodology for the characterization of dispersed organic matter in shales, and ultimately the search for and development of unconventional shale resources in the Karoo Basin and other similar basins impacted by volcanic activities. The specific objectives were to: (1) characterize the petrographic and geochemical evolution of oil-prone sedimentary organic matter in response to heat flow from magmatic emplacement, including changes to the optical texture, morphology, and chemical composition of hydrocarbon products; and (2) evaluate the effect of rapid thermal stress on the petroleum system of the Karoo shale reservoirs with a focus on gas retention. A combined analytical approach, consisting of light and electron microscopy (CLEM), programmed pyrolysis, and isotope ratio mass spectrometry (IRMS) was employed to determine organic abundances, identify maceral types, and characterize thermal conversion (secondary) products, such as volatile oil, solid bitumen, natural coke (carbon residue from short-term heating of organic matter), and pyrolytic carbon (vapor-deposited carbon from high-temperature cracking of methane).

2. Geological setting

The South African shale gas is hosted in the Lower Permian organic-rich Ecca Shale in the southern half of the Karoo Basin (Fig. 1). The basin is interpreted as a compressional retroarc foreland system that developed during the shallow-angle subduction of the paleo-Pacific plate beneath the Gondwana supercontinent. Karoo-aged sediments are also found in other continents that were once part of the Gondwanaland, including South America, Australia, Antarctica, Falkland Islands, and India (Fig. 1A), as well as in subbasins within southern Africa (Anderson and Schwyzer, 1977; Faure and Cole, 1999; Johnson et al., 2006). Sedimentation in the basin started in the Late Carboniferous at c. 300 Ma and continued until the initial stages of the breakup of Gondwana in the Jurassic at c. 183 Ma (Johnson et al., 2006; Geel et al., 2015; de Kock et al., 2017). Although the sedimentary fill of the Karoo Basin accumulated under the influence of climatic and tectonic controls, climate provides an overall trend for the sedimentation. The earliest deposits were glacial sediments (Dwyka Group) and sandstones and shales of the Ecca Group, which reflect a general shift from cold to semi-arid conditions during the Late Carboniferous to Early Permian when Gondwana was located at high southern latitudes and covered by a thick ice sheet (Johnson et al., 2006). Progressively warmer climates with fluctuating precipitation as Gondwana drifted towards more temperate climates during the rest of the Karoo times are represented by the deposition of the interbedded sand- and mudstones of the Beaufort and Stromberg groups (Johnson et al., 2006; Geel et al., 2015).

Karoo sedimentation was terminated by extensional tectonics associated with the initial stages of Gondwana fragmentation and coeval extrusion of basaltic lavas of the Karoo Large Igneous Province, represented by the ca. 1.4 km thick Drakensberg Group (Duncan et al., 1997; de Kock et al., 2017). The intrusions of dolerite sills and dikes into the Karoo sedimentary sequence represent the roots and feeders of the Drakensberg Group. The Jurassic volcanic activity, which was connected to the breakup of the Gondwana supercontinent and the formation of the South Atlantic (Johnson et al., 2006), was also widespread in other southwest Gondwanan basins, including the Parana Basin in Brazil (e.g., Triguis and Arano, 1995). The Karoo dolerite sills and dikes occur throughout the basin, except south of the so-called dolerite line (Fig. 1B). However, they preferentially intruded the organic-rich units, which are represented in the southern part of the basin by the Lower Ecca shales and in the northern part by the coal-bearing Vryheid Formation, because of the low competence of these organic-rich units. The Karoo dolerites broadly fall under the basic group (tholeiitic basalts to basaltic andesites) and comprise mainly plagioclase, pyroxene, and

olivine (Jourdan et al., 2006); however, more evolved sills are locally present (Neumann et al., 2011).

During the Cretaceous, large-scale sediment exhumation occurred in the southern part of South Africa, coeval with the development of large rift onshore and offshore basins, which was associated with the breakup of the Gondwana supercontinent and opening of the South Atlantic (Macdonald et al., 2003; Tinker et al., 2008). It is estimated that up to 5 km of sediment was eroded from the Cape fold-thrust Belt and up to 6–7.5 km from the Karoo Supergroup during two pulses of exhumation in the early and mid to late-Cretaceous (Tinker et al., 2008).

Three major organic maturity provinces occur in the basin as presented in Fig. 1B (Rowsell and De Swart, 1976; Cole and McLachlan, 1991, 1994; Geel et al., 2015; de Kock et al., 2017):

1. The southern part of the basin located roughly south of latitude 31° 30′ S is considered thermally overmature, with local features of incipient metamorphism caused by deep sediment burial and associated high temperature from the down-warp that resulted from the formation of Cape fold-and-thrust belt.
2. The central part of the basin lying roughly between latitude 31° 30′ and 30°S is overmature with respect to oil generation, consistent with the preservation of dry gas. There are no indications of metamorphism, except in the contact aureoles of igneous intrusions. The maturity stage of this region reflects the combined effect of deep burial and thermal stress from igneous intrusions.
3. The area north of latitude 30°S is in the peak oil stage, consistent with the preservation of oil and wet gas, apart from the contact aureole zones of intrusions.

Several oil and gas shows were recorded in various areas of the basin, particularly in areas north of latitude 30°S (e.g., Rowsell and De Swart, 1976; Cole and McLachlan, 1991; de Kock et al., 2017). However, their origin (whether due to the thermal impact of intrusions or burial-induced maturation) is unclear because maximum sediment burial and the emplacement of magmas are nearly synchronous within the second

Fig. 2. A. Outcrop image taken with DJI Mavic 2 Pro drone showing two laterally continuous dolerite sills that preferentially intruded the upper and lower contacts of the Whitehill Formation in Loeriesfontein (−31°16′01″, 19°42′58″). B: The upper sill is up to 16.42 m and consists of two stacked intrusions, which can be distinguished based on horizontal contacts and change in the plane of their cooling joints. C: Shale layers in contact with the lower sill are folded. D: Outcrop of the Whitehill Formation in Loeriesfontein (−31°06′46″, 19°28′51″), showing the characteristic change in lithology of the shale in contact with the dolerite sill. E: Hand-specimen of coked shale near the contact with the upper sill at A. F: Outcrop image showing chaotic vertical and horizontal fractures rooted in the aureole zone of the upper sill and filled with solid bitumen, pyrolytic carbon, and calcite, running parallel to bedding in the Whitehill Formation. G: A relatively unweathered outcrop of the Whitehill Formation unaffected by intrusion at −30°56′50″, 19°25′40″. H: Close-up image of hand specimen of black thinly laminated Whitehill shale at G.

and third thermal maturity regions (Fig. 1B).

3. Samples and analytical methods

3.1. Shale samples and sill distribution

The material for the present study was collected from two equivalent stratigraphic sections of the Whitehill Formation in the Loeriesfontein area (Figs. 1B, C, 2). In addition to excellent laterally continuous exposure of relatively unweathered rock, this location enables sampling to document the petrographic effects of igneous intrusions on the evolution of oil-prone sedimentary organic matter, and thence the shale resource system. Several aspects of this location are noteworthy: firstly, Oelofsen (1981) has shown that sedimentary facies and biozones within the formation are fully represented in this area of the basin. Furthermore, like other dolerite-impacted areas in the basin, small (up to 12.7 km^2) dolerite-free areas, called pans (Cole and McLachlan, 1994) are present in this locality. Thus, one of the sampled sections is unaffected by intrusion and serves in this analysis as background. The non-presence of intrusions in this section is also confirmed by the absence of brown dolerite boulders, which results from weathering of dolerites and is omnipresent in areas where previous intrusions have been removed. Also, two water boreholes located some 9 km from the sampled location (Fig. 1C) drilled in 2020 to a depth of 178 m to the Dwyka Group did not intercept any intrusion. The second stratigraphic section was intruded by two dolerite sills with average thicknesses of 10.7 and 9.3 m emplaced at the upper and lower contacts of the formation, respectively (Figs. 1C, 2). The two sills are laterally persistent throughout the study area and are also intercepted by boreholes G39980 (−31°30′16″, 19°41′45″) and G39856 (−31°29′22″, 19°54′15″), some 41 km southeast of the study location. The dolerite sills can be identified by their sharp contact with the host shales, reddish to dark brown color, and spheroidal weathering (Fig. 2A-D). The two sills are undulating and display similarity in both orientation and geometry, thickening and tapering at the same locations. In places, the upper sill bifurcates into several thin (0.18–1.77 m thick) closely spaced sills.

Previous studies of organic matter in the formation in adjoining areas of the basin with no sills are at peak oil maturity stage with vitrinite reflectance of 0.7–0.9% and still contains remnants of primary organic matter (Cole and McLachlan, 1991; Aarnes et al., 2011; Chukwuma et al., 2021), thereby allowing the impact of the sills on precursor-product relationships to be assessed. The effect of varying sill thicknesses and vertical heterogeneities can also be evaluated.

High-resolution sampling (5–25 cm intervals) was carried out across the complete vertical transect of the formation in two locations. The first location (LOER1; −30°56′50″, 19°25′40″) is within the area with no intrusions, and the second (LOER2; −31°06′46″, 19°28′51″) is intruded by the two sills. Sampling was done using a STIHL *E*-Z Core Rock Drill fitted with a Pomeroy 40 × 2.5 cm. Hand specimens were also collected where possible. The samples are crisp black and laminated (Fig. 2H) and give out a strong hydrocarbon stench when broken. Some exuded oil in form of droplets on the surface of the polished whole-rock. Also, the similarities of their TOC content to those from previous studies (e.g., Rowsell and De Swart, 1976; Cole and McLachlan, 1991; Geel et al., 2015; Chukwuma, 2017), as well as those from the recently drilled boreholes confirm the unweathered nature of the samples. The samples are given a five-digit code that represents their stratigraphic section and height from the base of the shale. For example, 14,088 is sampled from the first stratigraphic section (LOER1) at 40.88 m from the base of the formation.

3.2. Analytical methods

3.2.1. Correlative reflected-light and scanning electron microscopy (CLEM)

Organic petrographic analysis was performed to identify macerals and to measure the reflectance of vitrinite (%Ro) and solid bitumen (%BRo) according to the ASTM Test Method for dispersed organic matter in sedimentary rocks (ASTM D7708–14), which recommends 30 measurements. Samples were set in epoxy resin under vacuum for 24 h, and the blocks were subsequently ground with 400 and 600 grit papers and polished with 1.0 and 0.06 μm alumina cloth, ensuring a scratch-free surface using a Struers Tegraforce automatic polisher following ISO 7404:2. Analyses were performed on a Zeiss AxioImager reflected-light petrographic microscope at ×500 under non-polarized white light (LED source) and immersion oil at a wavelength of 546 nm, and Hilgers Diskus Fossil software. The reflectance system was calibrated using 3.24% CZ (Cubic-zirconia) and 0.900% YAG (Yttrium-aluminium-garnet) reflectance standards under white non-polarized light and immersion oil (ISO 7404:5 and ASTM D7708–14). To enhance observation of the anisotropy of the organic components, the particles were also observed under cross-polarizers with a retarder plate (quarter-wave lambda plate) at ×1000. Maceral recognition and differentiation are primarily based on the reflectance, internal texture, morphology, intergrain relationship, and other optical properties of macerals, and following standard organic petrology methods (Taylor et al., 1998; Suárez-Ruiz et al., 2012; ASTM, 2014). A subset of samples ($n = 14$) was crushed to about 1.0 mm (maximum size) and solvent-extracted with an azeotropic mixture of dichloromethane-methanol (93:7 *v*/v) using the method of Radke et al. (1986) for approximately 72 h and the residues were also examined after drying, the aim being to evaluate the solubility of the organic matter.

The polished sections were coated with a thin layer of evaporated carbon and examined with a Zeiss MERLIN field-emission scanning electron microscope (FE-SEM). The FE-SEM is linked with an Electron Dispersive Spectroscopy (EDS) instrument and equipped with: (1) secondary electron imaging (SE) operated using an accelerating voltage of 5 kV, a sample current of 250 pA, and a working distance of 3 mm; (2) back-scattered electron (BSE) imaging operated using an accelerating voltage of 20 kV, a sample current of 11 nA, and a working distance around 9.5 mm; and (3) cathodoluminescence (CL) detectors. The FE-SEM was also operated under cryogenic settings, whereby samples held at cryogenic temperatures (−180 °C) by freezing in a pool of liquid nitrogen were quickly transferred into the FE-SEM chamber. This technique minimizes interference between individual shale constituents and phases, allowing both phase imaging and detection of constituents as small as 10 nm (Desbois et al., 2013). The general distribution and abundance of organic materials were examined using a swath of ten images captured at 100–20 μm horizontal field width, machine magnification of 3000-1500×, and pixel size of 5–20 nm/pixel using BSE/SE. Additional characterization and mineral component identification were made using BSE/CL/EDS with images captured at 20–2.0 μm horizontal field width at a magnification of 15,000-250,000× and pixel size between 20 and 2 nm/pixel.

3.2.2. Organic geochemical analyses

Samples for chemical analyses were ground to a powder (<70 μm) and decarbonated using HCl with 6 M concentration for 24 h at room temperature. The samples were then neutralized in deionized water by repeated washing until pH test was close to neutral (≥6.0), followed by drying in a vacuum oven at 30 °C. Programmed pyrolysis using a Rock-Eval 6 analyzer (Vinci Technologies, France) was performed to gain information about the TOC content, kerogen type, and maturity. The total carbon (TC) content was determined with a LECO CS-244 carbon/sulfur analyzer. Rock-Eval programmed pyrolysis was performed in duplicate following standard procedures, including temperature settings and heating ramp (Espitalié et al., 1985) at the Indian Institute of Technology, Bombay. The calibration of the instrument was performed using the 55.000 IFP standard and analytical reproducibility was better than 0.2%. The 14 solvent-extracted sample powders were also analyzed. The initial temperature of the pyrolysis oven was maintained at 300 °C for 5 min and then raised to 600 °C at a rate of 25 °C/min.

The oxidation phase of the pyrolysis experiments was conducted

with temperature conditions similar to the pyrolysis oven but was raised to a maximum of 850 °C. Maturity and source quality parameters derived from Rock-Eval pyrolysis (Table 1) include the following: (1) hydrogen index (HI, [S2/TOC] × 100, mg HC/g TOC), is the amount of hydrocarbons per gram TOC released from cracking kerogen and heavy hydrocarbons during temperature programmed pyrolysis at 300–600 °C, and thus represents the existing potential of source rocks to generate hydrocarbons. (2) Oxygen index (OI, [S3/TOC] × 100, mg CO_2/g TOC), namely the amount of CO_2 released from breaking carboxyl and other oxygen-containing compounds per gram TOC released at 300–390 °C. (3) Oil saturation index (OSI, S1 × 100/TOC, mg HC/g TOC), is the amount of free hydrocarbon per gram TOC released at 300 °C. (4) T_{max} (°C, temperature of the maximum S2 peak) is a measure of the thermal maturity an organic material has attained.

A subset of the decarbonated samples was analyzed for the carbon isotope composition of total organic matter following the procedure of Könitzer et al. (2012), using a Thermo Finnigan Delta Plus XL isotope ratio mass spectrometer (IRMS) in continuous flow mode connected to a zero-blank autosampler Costech Elemental Analyzer (EA). Measurements were conducted at the Stable Isotope Laboratory of Iowa State University and the Environmental Isotope Laboratory of the University of Waterloo. Approximately 30 mg of each sample was wrapped in a tin capsule and placed into the zero-blank autosampler, and then combusted in the EA. One full run comprised 49 positions (1 blank, 12 standards, and 36 samples). Reference standards (caffeine [IAEA-600], IAEA-N2, cellulose (IAEA-CH-3), and acetanilide [laboratory standard]) were used for isotopic corrections and to assign the data to the appropriate isotopic scale. Elemental concentrations were calculated using reference standards and the sample gas intensities. Corrections were done using a regression method. The stable isotope compositions are reported in the conventional delta-notation against the Vienna Peedee belemnite (VPDB) standard. The combined uncertainty (analytical uncertainty and average correction factor) for $\delta^{13}C$ is ±0.06‰ (VPDB).

4. Results

4.1. Distribution of organic abundance and geochemical composition in the section with no sill

The TOC content of 71 selected samples increases up-section from 0.9% in the lower section to 17% in the upper section of the Whitehill Formation which is unaltered by intrusions (Fig. 3; Table 1). TOC values are positively skewed with peak (mode) at 8.60% and average values at 8.49% (Fig. 3A). The HI and OI values range from 50 to 568 mg HC/g TOC (average of 228 mg HC/ g TOC) and 5 to 93 mg CO_2/g TOC (average of 21 mg CO_2/ g TOC), respectively.

Based on the pseudo van Krevelen discriminant charts for HI versus OI and HI versus Tmax (Fig. 3B, C), the organic assemblage can be regarded generally as dominated by Type II and possibly Type I kerogen. The pyrolysis T_{max} values show a rather wide variation, ranging between 429 and 471 °C (average of 448 °C). Much lower values of 429 and 431 °C were recorded in three samples of dolomite concretions with very low TOC and S2 values. Relative to the whole-rock, TOC content and S2 values of the solvent-extracted residues show a decrease of up to 33 and 27%, respectively (Table 1). Similarly, with the TOC content, the isotopic composition of organic matter ($\delta^{13}C_{org}$) is variable and shows a general up-section increase, ranging from −24.7‰ at the base to −15.5‰ VPDB at the top. Samples with high TOC contents typically show less negative $\delta^{13}C_{org}$ values. Some of these geochemical results from the stratigraphic section with no intrusion have been reported in previous studies that evaluated the sedimentology and diagenetic variations of this shale formation (Chukwuma et al., 2021, 2022) and are represented here for comparison with the sill-hosting section.

4.1.1. Petrographic composition of organic matter in the section with no sill

As expected of this Type II kerogen-dominated lacustrine black shale, the petrographically-recognizable organic assemblage (macerals) is dominated by solid bitumen with lesser concentrations of vitrinite and inertinite. Solid bitumen as used here represents thermal conversion products of the original oil-prone organic matter in sediments (kerogen) and it is without reference for solubility in organic solvents (Hackley et al., 2020). Under reflected white light at 500× magnification, solid bitumen is recognized by its gray surface and semi-translucence with internal white reflections from embedded pyrite and clay-sized minerals, groundmass, pore-filling and anastomosing textures, embayment by authigenic minerals, and isotopic and granular textures (Figs. 4, 5).

Solid bitumen occurs mostly as homogenous accumulations in the form of continuous bedding-plane parallel organic streaks that typically form elongated, anastomosing networks (> 200 μm in long dimension and > 20 μm in short dimension), which sometimes covered the entire length of the analyzed sections (Fig. 4A-E). This anastomosing solid bitumen network typically occurs in close textural association with clay-rich matrix and pyrite framboids and displays granular texture (Fig. 4A-E). In SEM-BSD images, solid bitumen networks are recognized by their dark gray appearance (Fig. 5). Solid bitumen networks can also take the form of a fracture-filling phase (Fig. 6A, B), where they completely or partially infill fractures. In places, a network of microcrystalline calcite-filled veins co-occurs with or adjacent to fracture-filling post-oil solid bitumen networks (Fig. 6C-D). Like solid bitumen, vitrinite appears gray under reflected white light, however, it is distinguished from solid bitumen by a higher and consistent reflectance and a more defined, blockier outline (Fig. 4G-K). Inertinite maceral is distinguished by substantially higher and variable reflectance and high relief (Fig. 4L).

The mean random reflectance of vitrinite particles ranges from 1.23 to 1.26%, with a standard deviation of 0.029–0.046% (Fig. 8A, C; Table 1), while the reflectance of solid bitumen ranges from 1.01 to 1.06% with a standard deviation of 0.097–0.139% (Fig. 8B, D; Table 1). Vitrinite components were not identified in most of the samples from the lower section, and as such only solid bitumen reflectance was measured in those samples.

4.2. The effects of igneous intrusions on organic matter

The effect of the sills on their host shales can be recognized in the field by a change in lithology from well-laminated black shales (Fig. 2G, H) to a more indurated light gray equivalent (Fig. 2C, D). Shale layers directly adjacent to the sills (up to 3.09 and 1.18 m for the upper sill) are also characterized by significant loss of organic material and locally folded laminae (Fig. 2C).

TOC values in the section of the WHF intruded by sills range from 0.05 to 9.39% (Table 2), with a sharp decline towards the sills (Fig. 9A; Table 2). Compared to the section without intrusions, this represents a decline of up to 43%. T_{max} values range from 456 to 609 °C, representing an increase of up to 29.3% relative to the section with no sill, however, these T_{max} values are unreliable because of the low S2 values of the samples. The isotopic composition of solid bitumen ($\delta^{13}C_{org}$) ranges from −18.16‰ to −27.09‰ VPDB. The $\delta^{13}C_{org}$ values systematically become more depleted within the contact zones of the sills, with a notable 3.1‰ depletion over a distance of about 12 m adjacent to the upper sill (Table 2).

The mean reflectance of vitrinite and solid bitumen range from 2.03 to 5.82% to 1.58–7.87%, respectively (Fig. 9B; Table 2). A strong positive correlation (R^2 = 0.97) exists between %Ro and %BRo values (Fig. 3D), showing that both vitrinite and bitumen reflectance are sensitive to extreme and rapid temperature changes.

As shown in Fig. 9B, the reflectance profiles for both solid bitumen and vitrinite particles from the upper and lower sills are asymmetric. Samples underlying the upper sill display higher reflectance values than those that overlie the lower sill, resulting in a more extended profile than that of the lower sill. Fig. 9B also shows that the decrease in reflectance

Table 1
Organic geochemical data measured across the stratigraphic section of a ca. 43 m thick outcrop of the Whitehill Formation in Loeriesfontein with no visible intrusion: Total organic carbon (TOC), total inorganic carbon (TIC), Rock-Eval/LECO TOC parameters (S1, S2, Tmax, HI, OI, OSI), carbon isotopes (d13C), and organic matter reflectance (vitrinite %Ro and solid bitumen %BRo).

Depth (M)	Lithofacies	Rock-Eval/LECO TOC									Isotope Composition			Organic Reflectance					
		Tmax (°C)	TIC (wt %)	TOC (wt%)	S1 (mg/g)	S2 (mg/g)	S3 (mg/g)	HI (S2/TOC)	OI (S3/TOC)	OSI (S1x100/TOC)	$\delta^{13}C_{org}$ (‰) VPDB	$\delta^{13}C_{dol}$ (‰) VPDB	$\delta^{13}C_{Cal}$ (‰) VPDB	Vitrinite (Ro)			Solid bitumen (BRo)		
														%	n	sd	%	n	sd
40.88		432	46.70	12.04	2.81	61.73	3.16	512.71	26.25	23.34	−18.30	14.86	10.60	1.26	35	0.03	1.01	29	0.14
40.88*		435		9.47	0.86	44.61	3.69	471.07	38.97	9.08									
40.60		457	46.13	13.32	1.93	50.05	3.77	375.75	28.30	14.49	−17.97	13.44	10.60						
40.15		443	40.88	12.14	4.03	44.22	1.91	364.25	15.73	33.20	−18.13	14.97	10.33						
39.40		443	41.33	14.48	2.95	37.04	1.44	255.80	9.94	20.37	−16.84	14.40	10.51	1.23	57	0.05	1.01	31	0.10
39.40*		447		10.51	1.04	23.11	1.53	219.89	14.56	9.90									
38.94		439	45.73	14.73	3.31	29.07	2.53	197.35	17.18	22.47	−17.46	15.33	9.68						
38.60		451	37.62	16.57	1.88	27.71	1.72	167.23	10.38	11.35	−15.51	14.86	11.80	1.23	41	0.04	1.02	37	0.14
38.60*		453		11.19	0.62	16.08	1.74	143.70	15.55	5.54									
38.40		449	37.71	14.96	2.01	47.01	0.23	314.24	1.54	13.44	−17.22	14.83	10.63						
37.19		435	33.50	12.66	1.79	39.97	2.76	315.72	21.80	14.14	−19.46	14.50	12.05						
36.70		437	42.57	15.01	2.64	18.47	1.34	123.05	8.93	17.59	−18.31	14.48	11.83						
36.40		449	40.42	14.69	1.98	48.59	0.93	330.77	6.33	13.48	−18.76	14.86	13.16	1.26	51	0.04	1.06	33	0.14
36.03		464	39.20	12.25	3.30	11.83	1.39	96.57	11.35	26.94	−20.18	12.55	12.27						
36.03*		471		8.94	1.15	7.36	1.46	82.33	16.33	12.86									
35.88		432	42.10	14.02	2.43	28.61	1.44	204.07	10.27	17.33	−19.06	14.42	12.80						
35.70		438	44.19	14.57	2.45	38.21	1.33	262.25	9.13	16.82	−20.31	14.03	11.70						
35.35		454	42.38	13.94	2.83	20.31	1.51	145.70	10.83	20.30	−20.11	14.31	12.31						
35.17	Upper carbonaceous-argillaceous interval	457	36.81	13.72	3.07	9.82	0.97	71.57	7.07	22.38	−18.21	12.97	12.84						
35.17*		452		11.32	3.04	8.88	1.01	78.45	8.92	26.86									
35.17		438	41.48	14.03	3.04	26.60	1.30	189.59	9.27	21.67	−18.37	13.92	12.70						
35.05		449	38.06	13.74	2.91	6.81	1.68	49.56	12.23	21.18	−19.55	13.30	13.66						
34.80		451	37.33	12.80	3.04	10.03	1.77	78.36	13.83	23.75	−19.59	12.70	13.97	1.22	33	0.07	1.04	38	0.18
34.80*		454		8.95	1.76	6.82	1.73	76.20	19.33	19.66				1.26	29	0.05	1.09	27	0.15
34.40		449	38.26	9.51	2.88	10.58	1.61	111.25	16.93	30.28	−20.22	11.46	12.71						
34.05		447	36.16	10.94	2.29	11.47	1.79	104.84	16.36	20.93	−20.09	12.90	14.03						
33.92		471	37.98	12.08	2.25	8.91	0.54	73.76	4.47	18.63	−20.06	12.60	11.46						
33.90		455	32.40	12.04	3.04	22.04	1.61	183.06	13.37	25.25	−20.31	12.41	13.81						
33.30		457	30.71	10.14	2.40	9.55	0.73	94.18	7.20	23.67	−20.11	11.06	13.74						
32.60		443	32.56	8.38	2.46	15.41	1.12	183.89	13.37	29.36	−20.44	10.10	13.72						
31.98		458	30.49	9.39	2.43	7.95	1.68	84.66	17.89	25.88	−20.83	10.79	13.97						
30.85		451	31.13	9.27	2.03	9.75	0.91	105.18	9.82	21.90	−20.42	9.93	14.09						
30.15B		457	27.17	8.21	1.98	10.52	0.83	128.14	10.11	24.12	−20.64	9.90	14.05						
30.15		459	26.12	7.18	2.31	11.06	1.05	154.04	14.62	32.17	−20.94	9.57	14.27						
30.15*		462		4.80	0.97	7.37	0.99	153.54	20.63	20.21									
29.40		431	25.81	7.11	2.19	7.48	1.58	105.20	22.22	30.80	−21.09	9.42	13.80						
29.18		429	24.46	6.36	2.71	35.41	1.35	556.76	21.23	42.61	−20.83	8.61	13.92						
28.20		461	22.03	5.95	2.68	29.01	1.47	487.56	24.71	45.04	−21.11	8.53	13.64						
27.90		457	22.40	6.97	2.18	4.27	1.61	61.26	23.10	31.28	−21.52	8.44	13.60						
27.18		451	25.81	8.12	1.83	46.08	1.26	567.49	15.52	22.54	−18.57	11.06	14.97	1.26	36	0.11	1.09	29	0.14
27.18*		456		6.87	0.79	31.43	1.36	457.50	19.80	11.50				1.23	32	0.09	1.10	37	0.18
26.22		462	24.64	7.70	1.70	14.48	1.33	188.05	17.27	22.08	−18.86	8.51	16.27						
24.90		448	18.89	7.55	2.68	16.42	0.71	217.48	9.40	35.50	−19.02	8.37	17.08						
22.35	Middle carbonaceous (dolomitic) interval	438	16.12	6.65	2.01	12.61	0.49	189.62	7.37	30.23	−19.35	8.46	15.54						
21.59		448	15.35	7.49	3.32	10.92	0.81	145.79	10.81	44.33	−18.76	8.87	16.12						
21.59*		453		5.81	1.75	6.81	0.87	117.21	14.97	30.12									
18.90		457	17.71	5.66	2.51	19.98	1.40	353.00	24.73	44.35	−20.64	8.33	16.02						
18.13		434	12.62	4.05	2.33	7.33	1.35	180.99	33.33	57.53	−22.10	8.26	15.02						
16.61		442	8.70	3.78	2.94	21.04	1.61	556.61	42.59	77.78	−21.09	8.2	14.54						

(*continued on next page*)

Table 1 (*continued*)

Depth (M)	Lithofacies	Rock-Eval/LECO TOC								Isotope Composition			Organic Reflectance					
		Tmax (°C)	TIC (wt %)	TOC (wt%)	S1 (mg/g)	S2 (mg/g)	S3 (mg/g)	HI (S2/TOC)	OI (S3/TOC)	OSI (S1x100/TOC)	$\delta^{13}C_{org}$ (‰) VPDB	$\delta^{13}C_{dol}$ (‰) VPDB	$\delta^{13}C_{Cal}$ (‰) VPDB	Vitrinite (Ro)			Solid bitumen (BRo)		
														%	n	sd	%	n	sd
15.70		451	6.46	3.65	1.38	3.84	0.87	105.21	23.84	37.81	−22.00	8.26	13.44						
14.03		447	6.90	3.82	1.08	3.07	0.39	80.37	10.21	28.27	−21.52	9.03	10.51						
14.03*		451		2.06	0.48	1.66	0.38	80.58	18.45	23.30									
12.90		449	5.30	2.94	1.39	5.77	0.87	196.26	29.59	47.28	−22.30	8.28	13.83						
11.60		439	4.60	5.78	1.06	18.62	1.82	322.15	31.49	18.34	−21.80	−8.6	−10.33						
11.60*		443		3.83	0.72	11.26	1.87	293.99	48.83	18.80							1.09	27	0.18
11.42		447	4.95	5.66	1.28	13.10	1.74	231.45	30.74	22.61	−22.32	−7.37							
10.58		452	3.12	4.96	1.62	12.73	1.35	256.65	27.22	32.66									
10.40		439	3.03	5.09	1.44	6.91	1.77	135.76	34.77	28.29	−22.97	−8.68	−9.66				1.10	32	0.21
10.40*		446		3.65	0.86	4.27	1.71	116.99	46.85	23.56									
9.35		433	4.29	4.38	1.39	11.04	0.83	252.05	18.95	31.74									
8.44		457	4.12	3.91	2.31	14.79	0.85	378.26	21.74	59.08	−23.38	−9.72	−9.70						
6.11	Lower siliceous interval	451	3.70	2.65	1.60	11.03	0.98	416.23	36.98	60.38							1.09	33	0.18
6.11		448		1.90	0.84	7.16	0.94	376.84	49.47	44.21									
4.59		442	3.03	3.26	2.51	6.68	0.57	204.91	17.48	76.99	−23.07	−9.41	−8.90						
3.10		449	2.29	2.08	2.38	6.04	1.28	290.38	61.54	114.42	−23.85	−11.04	−8.85						
1.60		464	3.11	4.38	1.96	8.66	1.54	197.72	35.16	44.75	−22.91	−11.06	−8.84						
0.47		458	3.19	2.93	1.55	14.17	1.09	483.62	37.20	52.90									
0.47*		462		1.77	0.86	8.74	1.03	493.79	58.19	48.59									
0.25		435	3.53	2.06	0.88	3.88	1.45	188.35	70.39	42.72	−24.71	−9.6	−7.2						
0.13		454	3.12	0.93	0.42	0.18	0.16	19.35	17.20	45.16							1.09	34	0.2

OSI = oil saturation index. * = solvent-extracted residue.

values of the organic particles away from the sills is gradual, and coupled with the absence of vitrinite particles in the lower section, renders it difficult to determine the exact thickness of the aureoles with precision based on organic reflectance.

The organic assemblage in heat-impacted samples is dominated by solid bitumen that typically developed along with the continuous networks of initially homogenous organic matter in the form of bedding parallel steaks/stringers, similar to the section with no intrusions. Here, inertinite and vitrinite likewise constitute a minor fraction of the organic component. With decreasing distance to the sills, distinctive changes to the petrographic attributes of solid bitumen, including morphology, optical texture, and isotope composition, were recorded. Thus, the petrographic texture and morphology of the solid bitumen particles were used in combination with the trend of organic reflectance to track the effect of the individual sills on organic matter alteration and explore ramifications for shale gas occurrence. These details are reported in the sections that follow.

4.2.1. Effects of the 10.7-m thick upper sill on the petrographic composition of organic matter

The thermal effect of the 10.7 m thick sill that forms the upper contact of the Whitehill Formation is reflected in changes in optical texture and morphology of the solid bitumen from irregularly oriented, fine-medium homogeneous, and granular textures (Fig. 4A-F) to angular, medium-coarse anisotropic grains (Fig. 7A-D). The textural anisotropy and angularity of the heat-affected solid bitumen networks become more pronounced with decreasing distance to the sill (Fig. 7C, D).

Moreover, in approaching the sill, petrographic observations show that the heat-affected solid bitumens become increasingly transformed into coke and pyrolytic carbon (Figs. 10, 11). The coke is recognized under reflected-light and oil-immersion by its mosaic texture, high anisotropy, presence of devolatilization pores, and high, variable coke reflectance, with average random reflectance ranging from 6.5 to 9% (Fig. 10D, G)- though values of up to 11.8% are also recorded, which are some of the attributes of intrusive-heat generated coke as listed in Goodarzi et al. (2019). The grain morphology and degree of anisotropy were further enhanced by observations made under cross-polars with a retarder plate (Figs. 10B, E, H, 11) and in SEM images (Fig. 10C, F, I). The size and number of devolatilization pores increase towards the sill, resulting in a dramatic increase in the mesoporosity of the coked shale (Fig. 10J-L). The textural attributes of the binder and filler components of the coke also show marked variability with decreasing distance to the sill (Fig. 11).

Pyrolytic carbon is recognized by its strong reflectance, with average random reflectance ranging from 9.2 to 16%, and growth characteristics as pore-lining and laminated textural forms in close relation with coke (Fig. 11E, F). The abundance and anisotropy of the pyrolytic carbon also increase steadily towards the sill.

Based on these observations, it was possible to subdivide the aureole into two subzones (Fig. 12): (1) an outer aureole zone of mild alteration where the solid bitumen networks become increasingly angular and anisotropic (Fig. 7A-D) but coke and pyrolytic carbon are absent; and (2) an inner aureole zone where the heat-affected solid bitumens are progressively converted into coke and pyrolytic carbon (Figs. 10, 11).

The thickness of the aureole zone of this sill is 25.79 m, representing almost 2.5 x the thickness of the sill. The inner aureole zone containing coke and pyrolytic carbon is 9.19 m thick. The reflectance of vitrinite (Fig. 10B) increased from 1.09 to 1.73% outside the aureole to 1.77–6.13%. Similarly, solid bitumen reflectance increased from 2.21 to 2.65% outside the aureole to 2.44–7.95% in the sill contact zone. In approaching the sill and within the inner aureole, $\delta^{13}C_{org}$ values decrease (become more negative) progressively from −24.18 to −27.12%, which represents a negative isotopic shift of 3.13‰ over a distance of 8.7 m within the inner aureole. The highest shift in $\delta^{13}C_{org}$ values was recorded in the samples enriched in pyrolytic carbon-filled

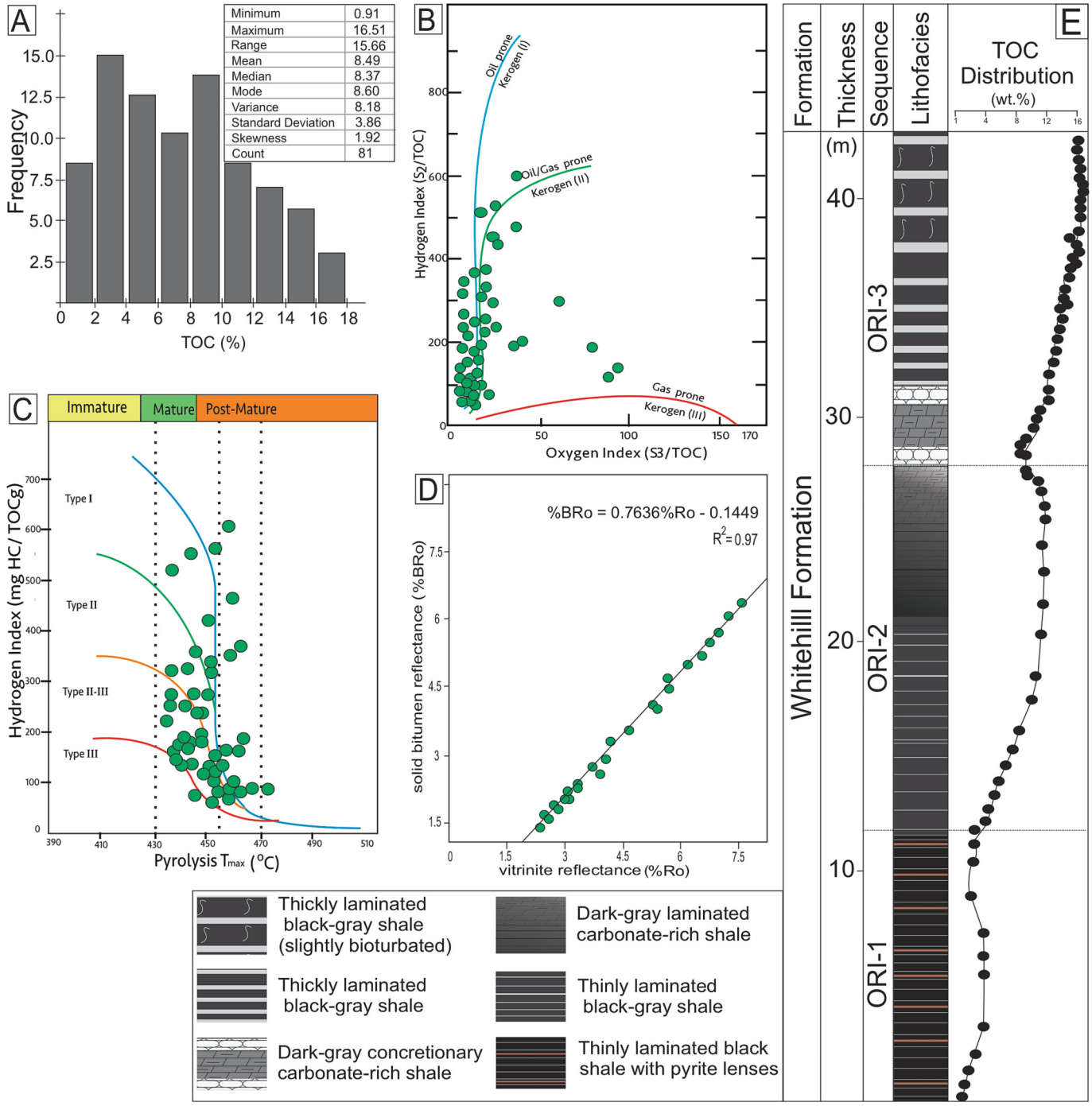

Fig. 3. A: Histogram of TOC values of the Whitehill Formation. The distribution of TOC values is positively skewed and consistent with a lognormal distribution. B: Modified van Krevelen HI vs OI kerogen type pyrogram. C: HI vs Tmax maturity pyrogram of the samples. Note that the least mature organic matter in the samples is in the peak-oil maturity window (Ro of 0.98%), suggesting that these Rock-Eval data do not strictly identify the type of organic matter initially present. D: Correlation between the reflectance of vitrinite and solid bitumen in the stratigraphic section of the formation intruded by dolerite sills. E: Stratigraphic distribution of lithofacies and total organic carbon content in a section of the Whitehill Formation with no igneous intrusion in Loeriesfontein.

veins, showing that the pyrolytic carbon is $\delta^{13}C_{org}$-depleted relative to adjacent organic matter.

4.2.2. Effects of the 9.3-m thick lower sill on the petrographic evolution of organic matter

The strata immediately surrounding the lower sill are lithified and brittle like those adjacent to the upper sill but do not display the obvious color change. The thermal effect of this sill can be observed over a distance of 14.7 m, which corresponds to just over 1.5 x the thickness of the sill. Over this distance, solid bitumen reflectance increased from 1.58 to 6.16%. In approaching the sill, $\delta^{13}C_{org}$ values decrease (become more negative) from −23.86 to −26.61%, representing a negative isotopic shift of 2.8‰ over a distance of 7 m.

The heat-affected solid bitumen networks show petrographic and geochemical changes with decreasing distance to the sill, similar to those observed in the upper sill, which also allowed the aureole to be subdivided into an outer and inner aureole at 11.9 and 2.8 m, respectively. However, in contrast to the upper aureole, only partial

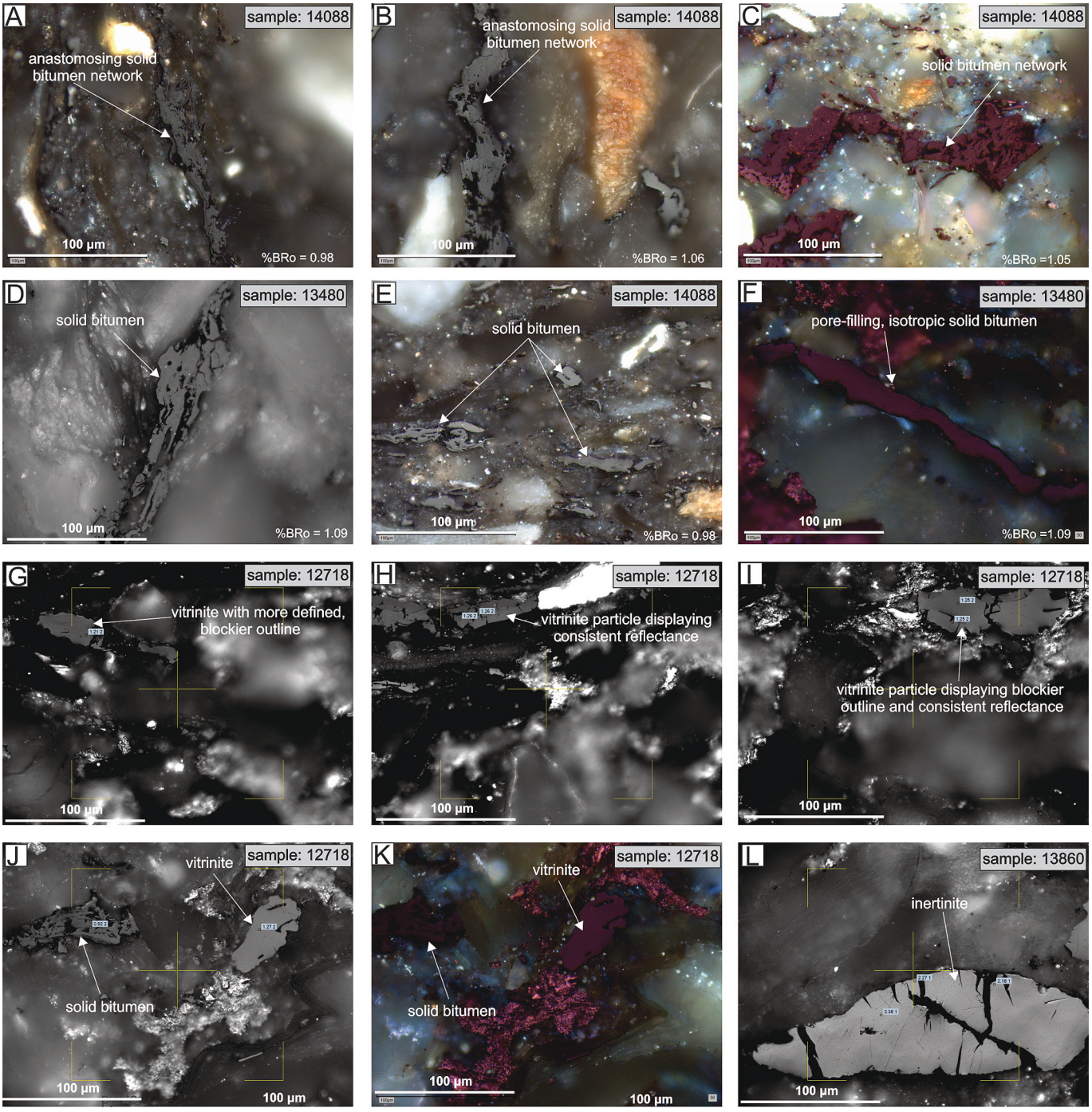

Fig. 4. Images of macerals in the Whitehill Formation taken using a Zeiss Axio Imager M2S reflected light microscope under oil immersion. The macerals were distinguished based on reflectance, morphology, and texture. Solid bitumen is identified by its gray surface, internal reflections from embedded authigenic minerals (e.g., pyrite), embayment by mineral grains, granular and isotropic textures, and pore-filling and anastomosing textures. Vitrinite displays a blockier outline and consistent reflectance, while inertinite exhibits variable reflectance and relief. A-B: Reflected colored light micrographs of a solid bitumen network with a granular texture and anastomosing outline, typically covering the length of the analyzed sections. C: Photomicrograph was taken under cross polars with a retarder plate to enhance textural features of solid bitumen network. D: Reflected white light micrograph of anastomosing solid bitumen network in close textural relation with a clayey matrix. E: Same as D, taken under cross polars with a retarder plate. F: Photomicrograph taken under cross polars with lambda plate showing isotropic pore-filling solid bitumen. G-I: Reflected white light micrographs showing vitrinite with a blockier outline and consistent reflectance readings. J: Reflected white light micrograph showing solid bitumen and vitrinite. K: Same as J taken under cross polars with a retarder plate. L: Reflected white light micrograph showing inertinite particle.

transformation of solid bitumen to coke and pyrolytic carbon was observed, and the reactive organic components of the shale matrix did not completely bind the non-reactive phases as observed in the aureole of the upper sill. The uncoked solid bitumen particles show a change from homogeneous to anisotropic textures and high reflectance. The optical texture of the coke and pyrolytic carbon did not show marked changes with decreasing distance to the sill. The coke grains generally exhibit incipient mosaic texture (Fig. 10A-C), while the strongly anisotropic folded coke grains and those with coarse circular and ribbon mosaic textures were not present here.

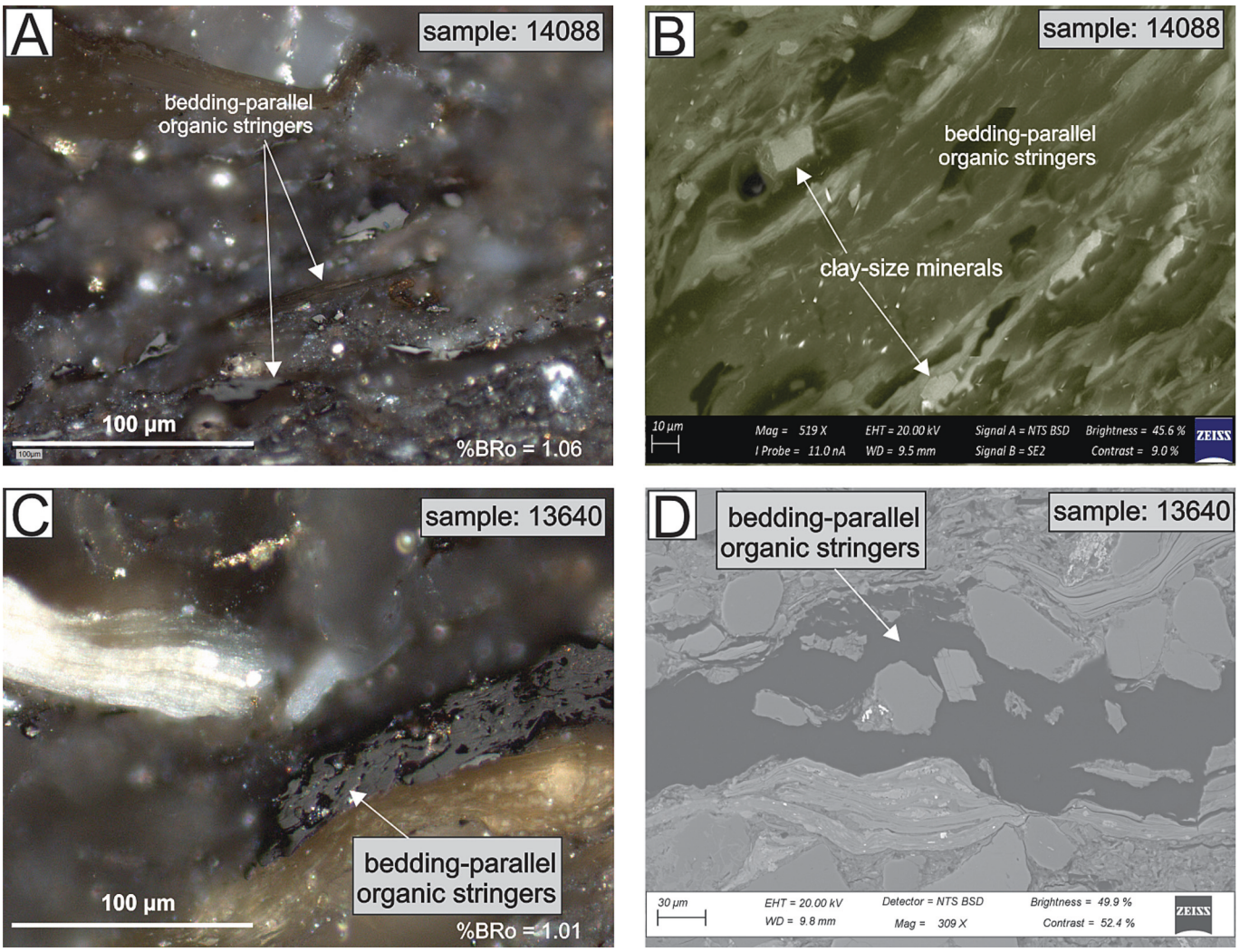

Fig. 5. Correlative reflected light (A, C) and SEM (B, D) micrographs of solid bitumen. A: Reflected white light micrographs of solid bitumen network in form of bedding-parallel stringers with a fine granular texture. B: SEM image of the same sample as A. C: Polarized white light with a retarder plate showing solid bitumen with isotropic pore-filling texture. D: SEM BSD image of the same sample as C.

5. Discussion

5.1. Origin and occurrence of thermal hydrocarbon products in the studied shale

Organic matter in the sections of the Whitehill Formation studied here is dominated by solid bitumen. The predominance of solid bitumen in these late oil- to gas-mature (0.98–1.26%Ro) samples is consistent with previous organic petrographic studies of shales at similar maturities, where solid bitumen is documented as the dominant organic fraction (e.g., Cardott et al., 2015; Harris et al., 2018b; Mastalerz et al., 2018; Hackley et al., 2021; Horsfield et al., 2021; Liu et al., 2022; Teng et al., 2022). These authors interpret the reduced abundance or complete absence of kerogen as the result of conversion to mobile petroleum and residual solid bitumen.

The reduced TOC content (by up to 33%) and S2 values (average of 27%) in the post-extraction residues relative to whole-rock samples recorded here is consistent with the interpretation that the solid bitumen phase consists of partially altered oil-prone Type II kerogen-rich organic matter and its maturation product. Thus, even though these samples are at peak- to late-oil generation state (%Ro of 1.23), a fraction of the organic matter could generate additional petroleum if subjected to increased maturity levels (Jarvie et al., 2007; Cardott et al., 2015; Mastalerz et al., 2018; Hackley et al., 2021; Liu et al., 2022).

Organic networks similar to those observed in this shale unit have been described in other shales, albeit without using the solid bitumen terminology. Bernard et al. (2012) recognized both hydrogen-rich (aliphatic) bitumens (derived from thermally altered organic matter) and nanoporous aromatic-rich pyrobitumen (derived from secondary thermal cracking of generated oil) in the samples of the overmature (1.45%Ro) Posidonia Shale. The respective descriptions of these two bitumen phases correspond to the solid bitumen terminology used here. The existence of this organic network, coupled with the high TOC content and moderate HI values of the samples is, therefore, consistent with the Whitehill Formation containing Type II oil-prone sedimentary organic matter at the time of its deposition (Cole and McLachlan, 1991; Visser, 1997; Chukwuma and Bordy, 2016).

5.2. The overall impact of igneous intrusions on organic matter maturation

The lower abundance or absence of solid bitumen networks in the sill-bearing section of the Whitehill Formation relative to the section containing no sill suggests that heat from the sills enhanced the conversion of original oil-prone organic matter to oil and the subsequent thermal cracking of that oil to gas. This observation is consistent with

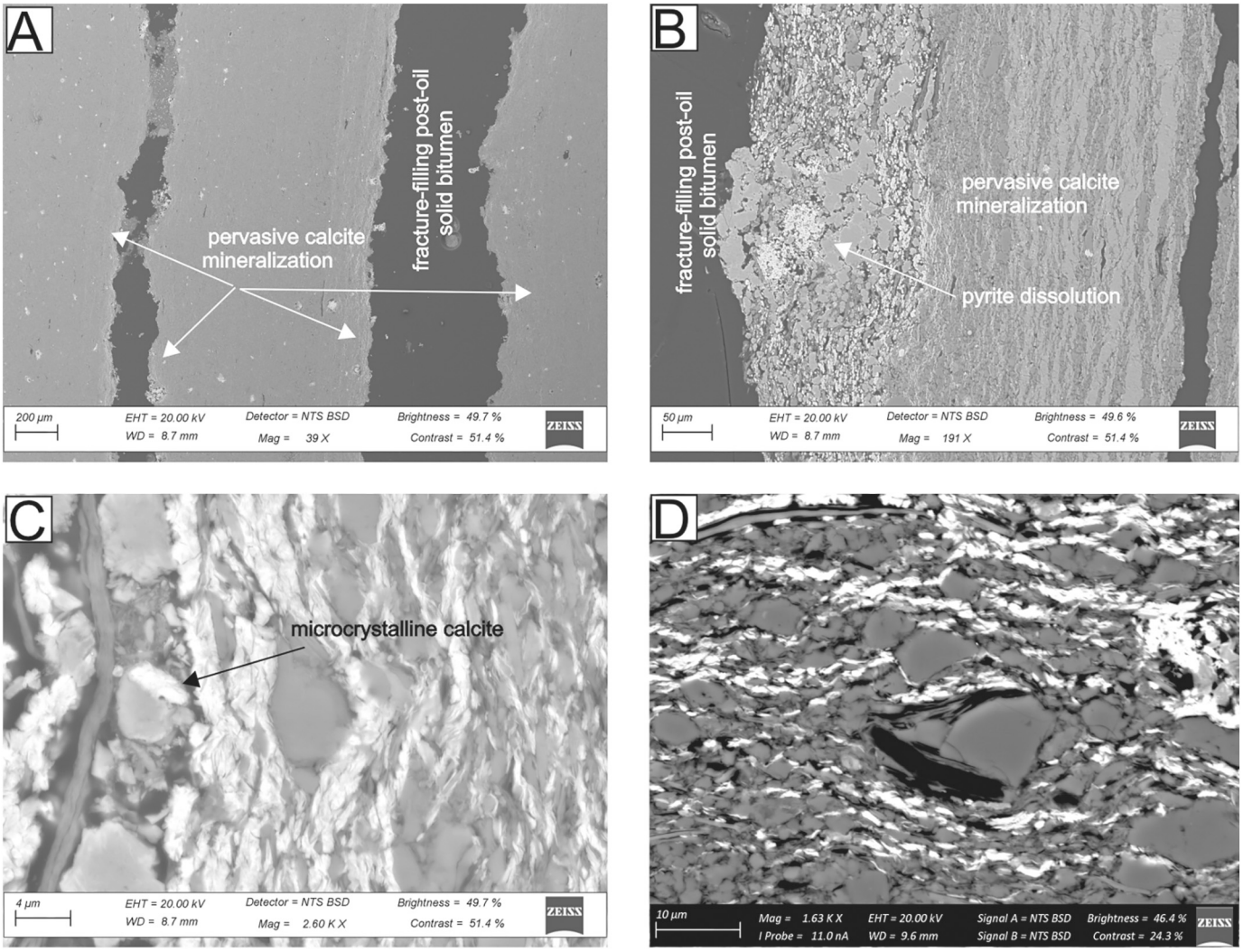

Fig. 6. SEM photomicrographs showing optical texture and morphology of fracture-filling post-oil solid bitumen in sample 21,035 in the sill-bearing section of the Whitehill Formation. A: Bedding-parallel fracture-filling post-oil solid bitumen network. Notice the pervasive calcite mineralization adjacent to the solid bitumen-filled features, which suggests that the fluid for calcite mineralization was supplied by hydrocarbon generation. Note also that this post-oil solid bitumen contains nanopores at higher magnification. B: Close-up image of A showing the calcite veining adjacent to the solid-bitumen-filled fracture. Notice effects pyrite of dissolution. C: Close-up image of C showing the microcrystalline texture of the calcite. D: Calcite mineralization in the shale matrix away from the solid bitumen-filled fractures.

the decrease of TOC and S2 values from peak values of 16.57% and 61.73 mg HC g^{-1} in the background samples to peak values of 9.39% and 8.07 mg HC g^{-1} rock, respectively, in the sill-bearing section. Hence, heat flow from the two sills emplaced at the lower and upper contacts of the formation increased the maturity of the entire stratigraphic section. Because only a few areas in the basin lack intrusions, these observations imply that the background organic maturity of this important formation in the basin was affected by the enhanced heat flow from the intrusions as predicted by Aarnes et al. (2011). Furthermore, within the aureoles, the hydrocarbon generation potential of the shales has been exhausted, as shown by low S2 values. As T_{max} is dependent on S2 values, this parameter becomes unreliable and cannot be used to establish the exact thickness of the aureoles.

5.3. Asymmetry of thermal aureole thicknesses

The thickness of thermal aureole zones generally varies with the thickness of intrusions, such that thicker intrusions produce wider thermally altered zone (Aarnes et al., 2011; Baker et al., 2015; Wang and Manga, 2015; Spacapan et al., 2018; Goodarzi et al., 2019). However, the thickness of the aureole zone of the two sills examined in this study appears to be asymmetrical (Fig. 9B). The aureole below the upper sill is estimated at 2.5 times the thickness of the sill, while that of the lower sill is about 1.6 times.

Spacapan et al. (2018) and Goodarzi et al. (2019) reported similar asymmetry of aureole thicknesses and interpreted it to represent the effect of successive events of magma emplacement, where the first magmatic event increased the background temperature of the host rock prior to the succeeding events (e.g., Hanson and Barton, 1989; Raymond and Murchison, 1989). The model of Aarnes et al. (2011) also demonstrates how higher background temperatures resulting from early intrusions retard the cooling of subsequent intrusives due to lower thermal gradients between the sill and the host-rock aureole. Key observations such as the overall similarity in the physical aspects (color, texture, weathering attributes, and orientation) of the two sills over 10s of km (Fig. 2A, B) suggest synchronous emplacement. However, Fig. 2B shows that the upper sill consists of two stacked intrusions, which can be distinguished by horizontal contact and a slight change in the vertical planes of their cooling joints. Thus, the possibility of additive heat from multiple emplacement events cannot be overruled.

Table 2
Organic geochemical data measured across the stratigraphic section of a ca. 54 m thick outcrop of the Whitehill Formation in Loeriesfontein intruded by two dolerite sills: total organic carbon (TOC), total inorganic carbon (TIC), Rock-Eval/LECO TOC parameters (S1, S2, Tmax, HI, OI, OSI), carbon isotopes (d13C), and organic matter reflectance (vitrinite %Ro and solid bitumen %BRo).

Depth (M)	Distance from sill	Zone of Alteration	Rock-Eval/LECO TOC								Isotope Composition		Organic Reflectance					
			Tmax (°C)	TOC (wt%)	S1 (mg/g)	S2 (mg/g)	S3 (mg/g)	HI (S2/TOC)	OI (S3/TOC)	OSI (S1x100/TOC)	$\delta^{13}C_{org}$ (‰) VPDB	$\delta^{13}C_{Cal}$ (‰) VPDB	Vitrinite (Ro)			Solid bitumen (BRo)		
													%	n	sd	%	n	sd
10.7 m thick upper dolerite sill																		
53.04	3.04		608	0.05	0.07	0.10	0.13	200.00	260.00	140.00	−26.53	−9.73						
52.88	3.20		609	0.13	0.07	0.15	0.30	115.38	230.77	53.85	−27.09	−9.51				7.92	17	1.12
52.55	3.53		602	0.15	0.06	0.11	0.32	73.33	213.33	40.00		−11.29				7.87	53	0.29
51.60	4.48		607	0.29	0.05	0.16	0.23	55.17	79.31	17.24	−26.46	−11.26				7.95	31	0.35
51.25	4.83		595	0.18	0.04	0.13	0.08	72.22	44.44	22.22	−26.88	−10.33				7.81	35	0.29
50.73	5.35		593	0.12	0.04	0.17	0.08	141.67	66.67	33.33						7.74	26	0.33
50.00	6.08		604	0.39	0.08	0.16	0.33	41.03	84.62	20.51	−27.12	−9.60				6.83	12	0.17
49.63	6.45		598	0.13	0.05	0.11	0.31	84.62	238.46	38.46	−25.57	−10.45				6.72	49	0.53
48.12	7.96	Upper aureole zone (with coke	577	0.72	0.04	0.49	0.51	68.06	70.83	5.56								
48.40	7.68	and pyrolytic carbon)	602	0.69	0.15	0.43	0.12	62.32	17.39	21.74	−25.05	−9.61				6.67	61	0.30
47.09	8.99		583	0.72	0.18	0.64	0.20	88.89	27.78	25.00	−24.79	−10.05				6.25	49	0.09
46.70	9.38		594	0.93	0.21	1.02	0.40	109.68	43.01	22.58	−24.81	−9.19						
46.40	9.68		607	1.46	0.40	0.71	0.30	48.63	20.55	27.40	−23.55	−9.16				5.42	25	0.15
46.03	10.05		549	1.67	0.40	0.71	0.30	42.51	17.96	23.95		−8.27						
45.38	10.70		532	2.11	0.11	0.48	0.17	22.75	8.06	5.21								
44.80	11.28		526	2.50	0.60	0.81	0.43	32.40	17.20	24.00	−22.64	−8.84	5.82	32	0.28	4.56	36	0.31
44.12	11.96		501	3.27	0.83	1.14	0.19	34.86	5.81	25.38	−24.04	−8.70				4.13	36	0.29
43.85	12.23		481	3.20	3.50	4.65	1.51	145.31	47.19	109.38	−24.18	−8.01	5.19	28	0.35	3.87	58	0.16
42.97	13.11		485	2.90	2.40	4.13	0.82	142.41	28.28	82.76	−23.96		4.42	29	0.23	3.19	33	0.37
42.40	13.68		502	4.14	1.17	3.35	0.32	80.92	7.73	28.26								
42.18	13.90		463	4.40	2.60	3.15	0.27	71.59	6.14	59.09	−21.14							
41.70	14.38		463	4.78	1.71	2.35	0.52	49.16	10.88	35.77	−21.89	−7.84	3.98	34	0.19	2.55	37	0.34
38.80	17.28	Lower aureole zone (angular	494	5.51	2.80	2.37	0.63	43.01	11.43	50.82	−19.94		3.22	29	0.19	2.36	41	0.41
36.35	19.73	solid bitumen, incipient coke)	487	5.83	2.85	6.14	0.41	105.32	7.03	48.89								
34.42	21.66		469	7.71	2.41	5.94	0.84	77.04	10.89	31.26	−20.57	−7.79						
34.05	22.03		494	7.63	3.39	8.07	1.71	105.77	22.41	44.43	−21.03	−7.32	3.10	37	0.18	2.06	32	0.27
33.92	22.16		471	6.81	4.25	7.26	0.54	106.61	7.93	62.41	−20.06	−8.10						
33.76	22.32		485	7.04	3.04	4.78	1.61	67.90	22.87	43.18	−20.44							
33.25	22.83		491	6.43	2.42	6.29	0.73	97.82	11.35	37.64	−20.63		2.83	28	0.14	1.92	37	0.31
32.60	23.48		483	5.75	2.80	3.63	1.12	63.13	19.48	48.70	−21.17							
31.85	24.23		471	9.39	2.21	5.44	1.17	57.93	12.46	23.54	−20.88	−7.37	2.69	36	0.23	1.87	41	0.35
31.44	24.64		477	6.58	7.83	6.14	0.58	93.31	8.81	119.00		−7.59						
30.75	25.33		469	4.17	4.86	5.52	0.86	132.37	20.62	116.55		−8.04						
30.15	25.93		479	5.91	2.17	0.54	1.05	9.14	17.77	36.72	−20.60	−7.83	2.59	31	0.18	1.74	50	0.28
29.81	26.27		472	4.80	3.52	4.43	0.99	92.29	20.63	73.33								
29.40	26.68		461	6.94	2.91	6.32	1.05	91.07	15.13	41.93	−21.11							
29.12	26.96		469	6.11	2.71	3.18	1.37	52.05	22.42	44.35	−20.78							
28.20	27.88		471	5.95	1.96	4.01	1.71	67.39	28.74	32.94	−19.72		2.29	28	0.31	1.68	31	0.33
27.77	28.31	Heat unaltered zone	474	4.97	2.15	4.29	1.71	86.32	34.41	43.26	−21.02							
27.35	28.73		461	6.05	1.83	6.19	1.68	102.31	27.77	30.25			2.05	32	0.24	1.61	29	0.27
27.12	28.96		456	5.33	0.79	3.79	1.25	71.11	23.45	14.82			2.03	27	0.26	1.59	21	0.28
26.42	26.42		462	4.07	1.70	4.84	1.38	118.92	33.91	41.77	−18.16	−8.03	2.09	28	0.31	1.58	31	0.33
24.90	24.90		458	4.58	2.68	6.33	0.76	138.21	16.59	58.52	−19.48	−7.78	2.27	37	0.17	1.59	27	0.27
22.35	22.35		467	4.83	2.01	2.61	0.43	54.04	8.90	41.61	−19.50	−7.55						
21.60	21.60		468	5.10	3.32	4.70	0.81	92.16	15.88	65.10	−18.86	−8.61						
20.18	20.18		463	5.81	1.75	3.66	0.87	62.99	14.97	30.12			2.30	35	0.24	1.61	27	0.25
19.90	19.90		477	5.66	2.51	5.87	1.40	103.71	24.73	44.35	−20.49	−8.02	2.38	28	0.31	1.68	31	0.33
18.55	18.55		474	4.05	2.33	3.33	1.35	82.22	33.33	57.53		−8.36	2.41	29	0.21	1.76	34	0.28

(*continued on next page*)

Table 2 (*continued*)

Depth (M)	Distance from sill	Zone of Alteration	Rock-Eval/LECO TOC								Isotope Composition		Organic Reflectance					
			Tmax (°C)	TOC (wt%)	S1 (mg/g)	S2 (mg/g)	S3 (mg/g)	HI (S2/TOC)	OI (S3/TOC)	OSI (S1x100/TOC)	$\delta^{13}C_{org}$ (‰) VPDB	$\delta^{13}C_{Cal}$ (‰) VPDB	Vitrinite (Ro)			Solid bitumen (BRo)		
													%	n	sd	%	n	sd
17.80	17.80		472	3.78	2.94	5.61	1.61	148.41	42.59	77.78	−21.04	−9.74						
17.25	17.25		474	3.65	1.38	3.14	0.87	86.03	23.84	37.81	−22.80	−9.13						
16.12	16.12		477	3.82	1.08	3.07	0.39	80.37	10.21	28.27	−22.52	−9.10	2.64	28	0.21	1.81	43	0.27
16.68	16.68		481	3.01	0.47	1.96	0.41	65.12	13.62	15.61								
15.90	15.90		489	1.97	1.42	3.35	0.89	170.05	45.18	72.08	−24.31	−10.32	2.88	27	0.21	1.87	43	0.27
14.60	14.60		487	2.78	1.06	1.86	1.70	66.91	61.15	38.13	−23.80	−9.69	3.11	32	0.36	2.18	27	0.30
13.85	13.85		483	2.82	0.72	1.26	1.97	44.68	69.86	25.53			3.32	24	0.42	2.39	29	0.29
12.50	12.50		481	2.66	1.28	3.19	1.74	119.92	65.41	48.12	−22.93	−10.53				3.16	28	0.18
11.80	11.80		482	1.96	1.62	1.83	1.35	93.37	68.88	82.65								
11.40	11.40		479	1.15	1.28	2.74	1.77	238.26	153.91	111.30	−22.97	−9.73						
10.90	10.90		496	1.65	0.81	2.21	1.71	133.94	103.64	49.09						4.03	28	0.18
10.35	10.35		511	0.85	0.07	0.10	0.53	11.76	62.35	8.24						4.27	43	0.23
9.63	9.63		509	1.03	0.07	0.15	0.30	14.56	29.13	6.80	−23.86	−9.84						
7.50	7.50	Aureole zone (with dispersed coke and pyrolytic carbon)	502	0.55	0.06	0.11	0.32	20.00	58.18	10.91						4.82	31	0.24
6.89	6.89		507	0.44	0.05	0.16	0.23	36.36	52.27	11.36								
5.50	5.50		505	0.48	0.04	0.13	0.18	27.08	37.50	8.33	−24.88	−10.31						
4.10	4.10		543	0.27	0.04	0.17	0.18	62.96	66.67	14.81	−25.73	−10.58				5.03	49	0.15
2.60	2.60		604	0.39	0.08	0.16	0.21	41.03	53.85	20.51	−25.94							
1.87	1.87		578	0.22	0.07	0.10	0.13	45.45	59.09	31.82						6.14	14	0.09
1.35	1.35		609	0.13	0.07	0.15	0.13	115.38	100.00	53.85	−26.07					5.97	23	0.19
0.55	0.55		602	0.15	0.06	0.11	0.22	73.33	146.67	40.00	−25.84	−10.75				6.16	21	0.20
0.24	0.24		606	0.14	0.05	0.14	0.23	100.00	164.29	35.71	−26.61	−10.71						
0.12	0.12		595	0.08	0.04	0.13	0.08	162.50	100.00	50.00								
0.08	0.08		609	0.05	0.03	0.10	0.06	200.00	120.00	60.00	−26.36							
9.3 m thick lower dolerite sill																		

Note that T_{max} is unreliable if S2 values are <0.2 mg/g.

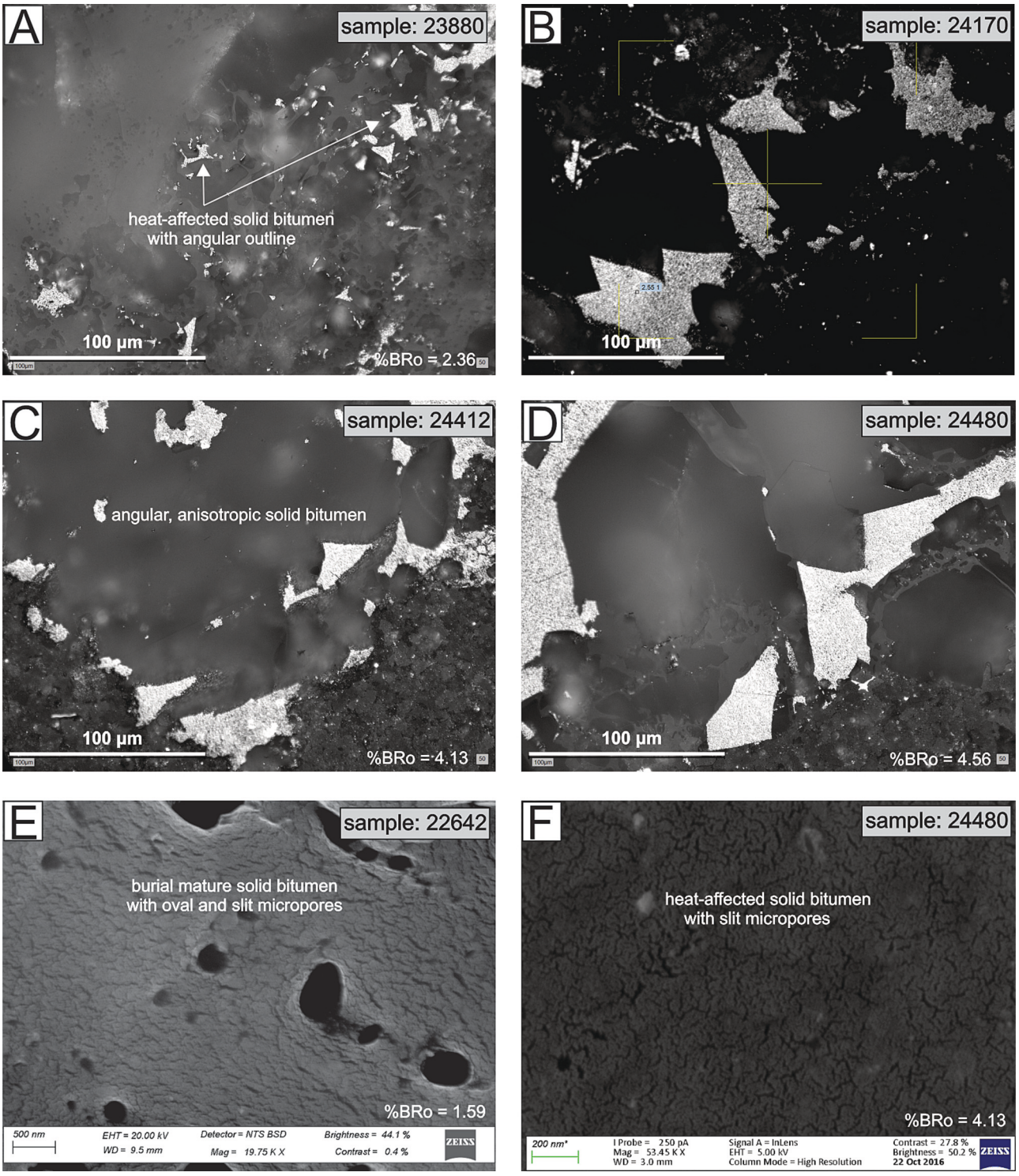

Fig. 7. A-D: Reflected white light and oil immersion photomicrographs showing the optical texture and morphology of heat-affected organic matter in the sill-bearing section of the Whitehill Formation. A-B: Shale matrix showing solid bitumen networks displaying angular outline. C-D: Dispersed heat-affected angular solid bitumen particles showing textural anisotropy. *E*-F: SEM images showing nanoporous solid bitumen. E: Heat-unaffected solid bitumen showing dual nanopore networks comprising larger oval pores and slit pores. F: Intrusive heat-affected solid bitumen network with drastically reduced to absent larger oval pores but dominated by slit pores at the scale of the SEM.

Another factor used to explain the asymmetry of aureole sizes is variability in the thermal conductivity of the host rocks (e.g., Raymond and Murchison, 1989; Nunn and Lin, 2002; Schimmelmann et al., 2009). Shales are known to be inherently heterogeneous, with individual formations composed of detrital silt and clay content, carbonate, biogenic silica, and organic carbon concentrations in stratigraphically variable proportions (e.g., Bohacs et al., 2013; Harris et al., 2018a). As a result, properties such as rock strength, porosity, and permeability tend to vary stratigraphically in shales (Harris et al., 2011). Thus, the thermal conductivity of individual shales, which depends on such factors as lithology, sediment consolidation, and water content, tends to vary, ranging from 0.7 to 1.2 Wm^{-1} °C (Nunn and Lin, 2002).

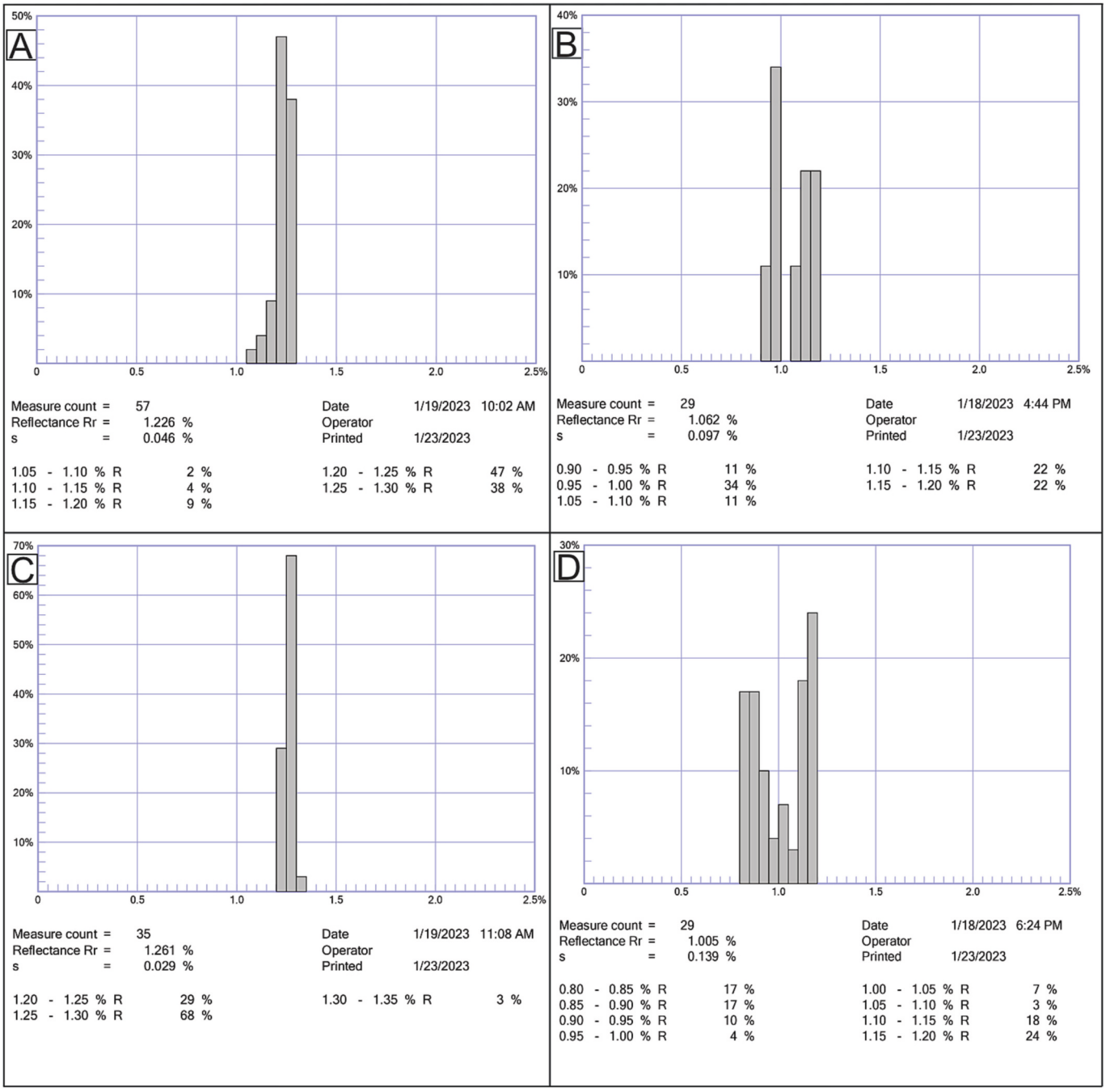

Fig. 8. Histogram showing the mean random reflectance of vitrinite (A, C) and solid bitumen (B, D) in the sections of the Whitehill Formation with no sill. A, C: Mean random vitrinite reflectance shows a consistent reading of 1.26%, with a standard deviation ranging from 0.029 to 0.046%. B, D: Mean random reflection of solid bitumen range from 1.01 to 1.06%, with standard deviation ranging from 0.097 to 0.139%.

The Whitehill Formation displays significant stratigraphic variability and has been subdivided into sub-units based on sedimentary features, including grain size and relative quartz, carbonate, clay minerals, and organic matter abundances (Cole and McLachlan, 1991; Visser, 1997; Chukwuma and Bordy, 2016). Marked increases in organic matter and clay content are documented in the upper section which has been shown to have resulted in higher water content relative to the lower section during the early burial stage of this formation (Chukwuma et al., 2021, 2022). The combination of these factors is likely to have resulted in variable thermal conductivity. We speculate that either additive heat flow from sequential emplacements or the increased abundance of both organic matter and clay minerals in the upper lithofacies would have caused the contact zones of the upper sill to remain at elevated temperatures for longer periods, thus resulting in the observed thicker aureole.

5.4. *The fate of organic carbon during sill-induced maturation*

The maturation of oil-prone sedimentary organic matter is dominantly a cracking and aromatization process, in which hydrogen and heteroelements are preferentially liberated as volatiles, and carbon is retained with graphite as the ultimate end product (Van Krevelen, 1993; Killops and Killops, 2005; Peters et al., 2005). The development of an increasingly granular texture in the naturally mature post-oil solid

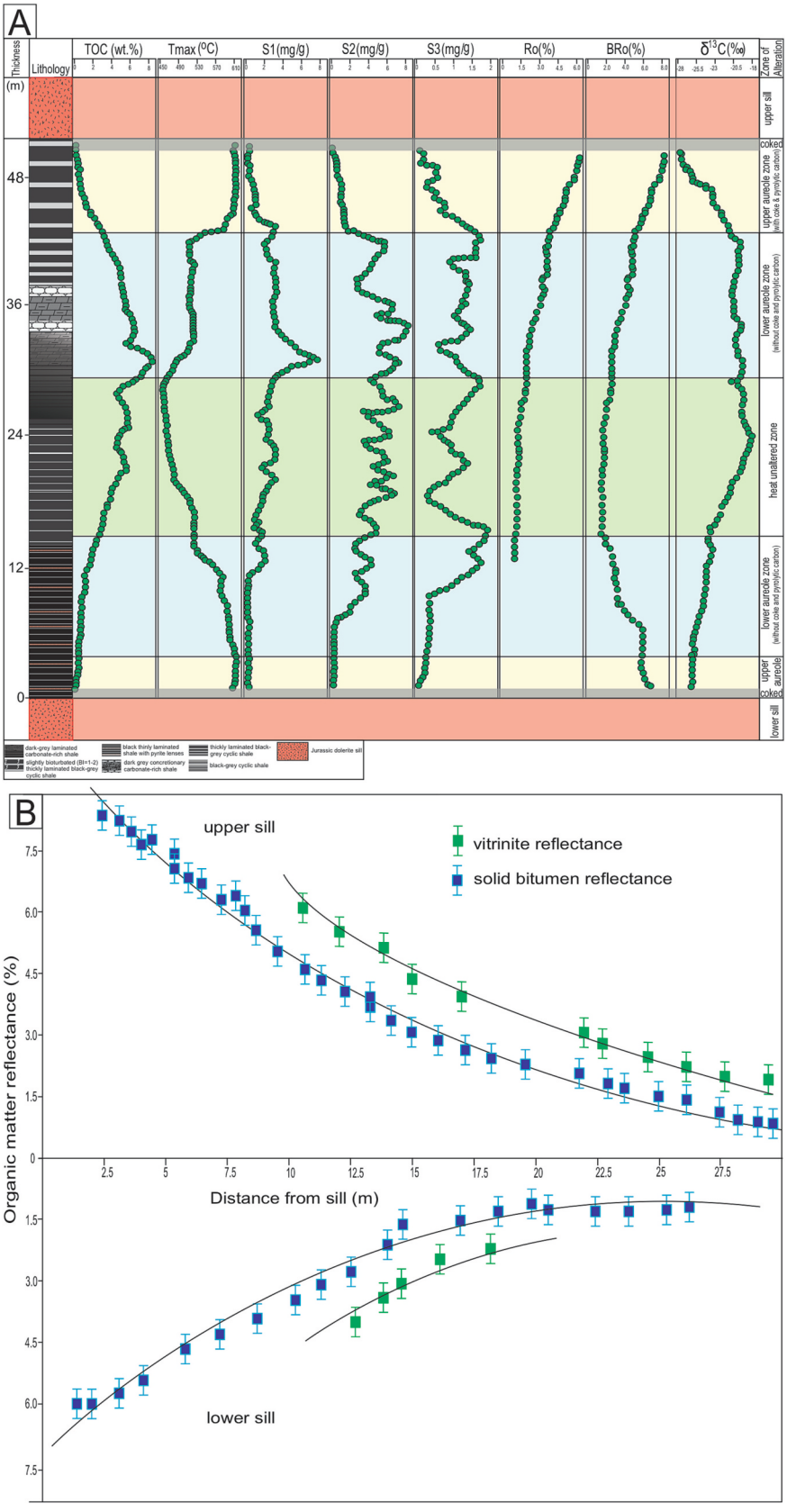

Fig. 9. A. Effect of upper and lower sill intrusions on the stratigraphic distribution of organic geochemical and petrographic composition of the Whitehill Formation (see Fig. 12 for interpretation). B: Vitrinite and solid bitumen reflectance measured across the stratigraphic section of the Whitehill Formation relative to the two sills to evaluate the effect of the latter on organic maturity. Relative to the thickness of the sills, the reflectance profiles of the upper sill are significantly higher and more extended than those of the lower sill, which implies asymmetrical aureoles.

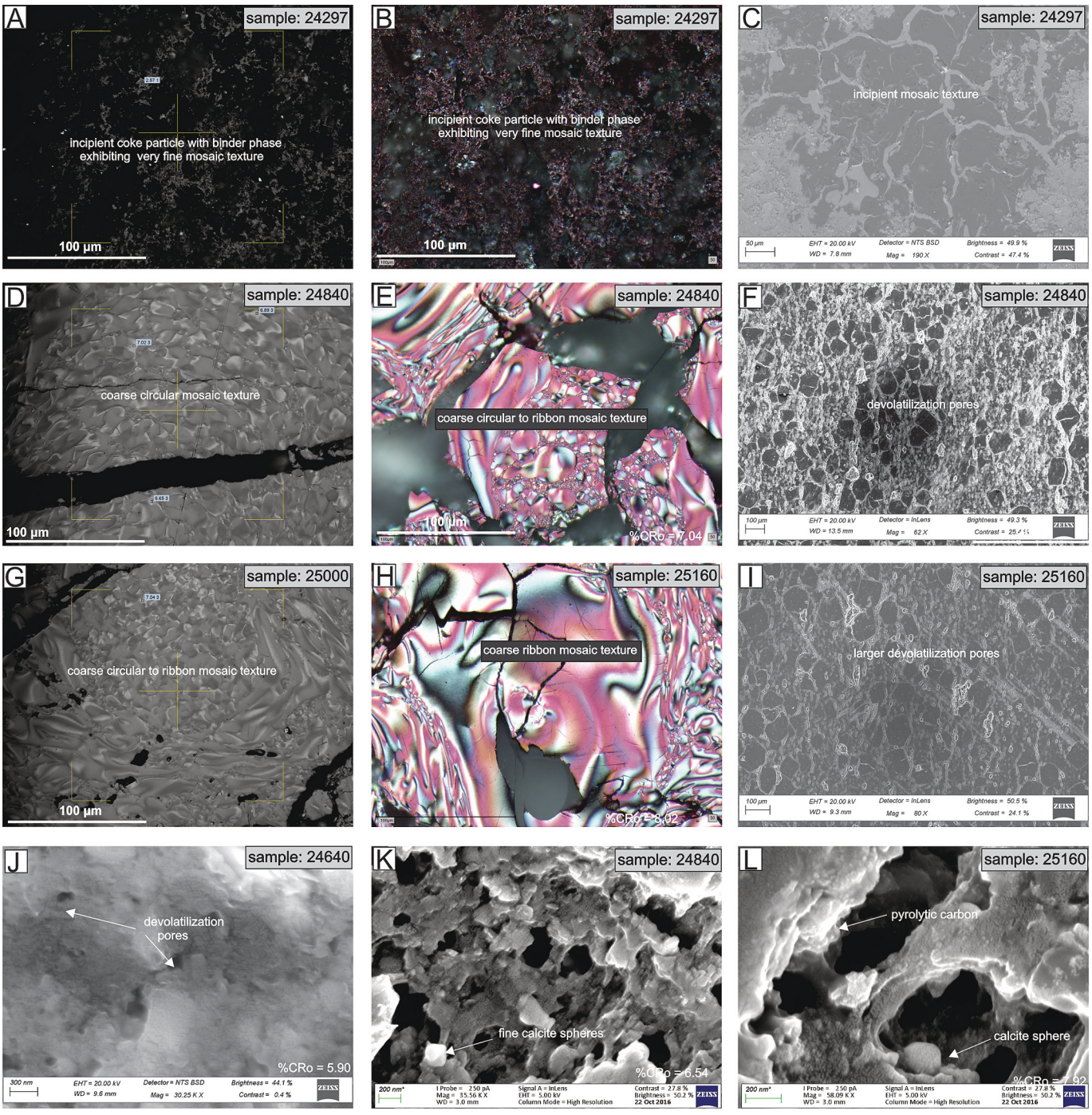

Fig. 10. A-I: Reflected light and oil immersion (A, B, D, E, G, H) and backscattered SEM (C, F, I, J, K, L) micrographs showing the differences in texture and morphology of coke grains in the sill-hosting section of the Whitehill Formation. A: Reflected white light micrograph of coke with incipient mosaic texture. B: The same sample as A, taken under cross polars with a retarder plate. C: SEM BSD of the same sample as A. D-I: Coke in the aureole of the upper sill show marked textural variability and increased anisotropy with decreasing distance to the sill. D: Reflected white light micrograph of coke exhibiting coarse circular to increasingly ribbon mosaic textures. E: The same sample as D, taken under cross polars with lambda plate. F: SEM Inlens of the same sample as D showing devolatilization pores and high coke porosity. G: Reflected white light micrograph of anisotropic coke in the shale layers adjacent to the upper sill, exhibiting increased ribbon mosaic texture. H: The same sample as G, taken under cross polars with lambda plate to enhance textural anisotropy. I: SEM micrograph of the same sample as G showing larger devolatilization pores and higher coke porosity. J-L: SEM micrographs show a systematic increase in the number and size of devolatilization pores in the coked shale with decreasing distance from the sill with J being the farthest and L closest to the upper sill. %CRo = coke reflectance.

bitumen with an increasing level of maturity observed outside the contact zones of the intrusions represents a better ordering of the molecular structure for graphitizing carbon.

The conversion of organic matter into coke and pyrolytic carbon within the contact aureole of the sills suggests that instead of carbon graphitization with increasing temperature, the heat from intrusions promoted the development of increased anisotropic, non-graphitized carbon. Volatiles were generated from the section intruded by sills, indicated by the pervasive presence of pyrolytic carbon and devolatilization pores in the coke grains (e.g., Aarnes et al., 2011; Goodarzi et al., 2019). This contrasts with the petrographic character of organic matter in the non-intruded section, although non-graphitized carbon is present

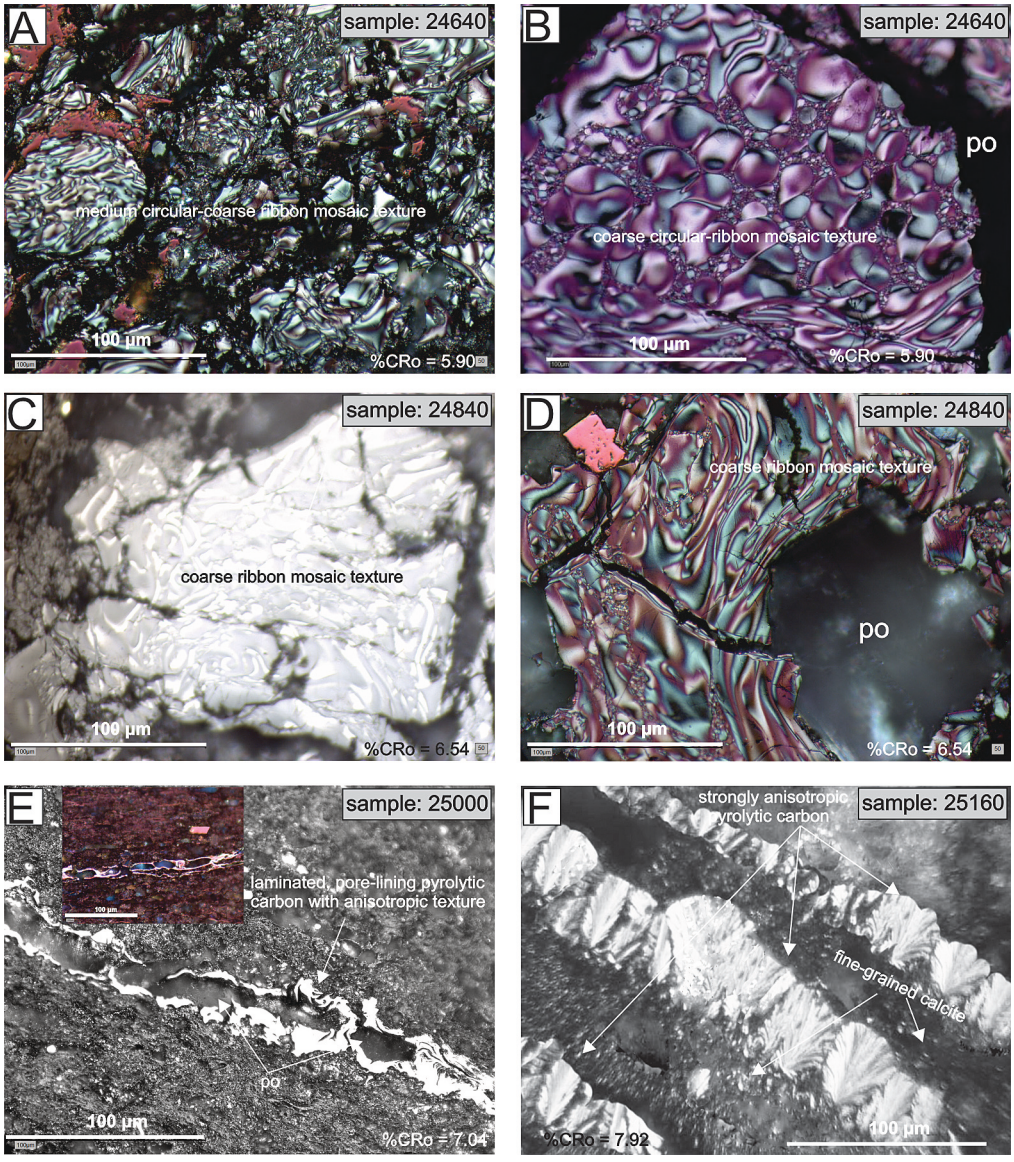

Fig. 11. Reflected light micrographs taken under oil immersion and cross-polars showing further relation between the binder and filler phases as well as pyrolytic carbon with decreasing distance to the sill, enhanced with a retarder plate. With decreasing distance to the sill, both the binder and filler components become increasingly anisotropic. A: Coke with medium circular mosaic texture, becoming increasingly ribbon towards the left, and dominated by isotropy of both binder and filler components. Observe porosity (Po). B: Coke is dominated by coarse circular and to a lesser extent coarse ribbon mosaic textures, isotropic filler, and anisotropic binder phase. C: Coke with coarse ribbon mosaic texture and anisotropic filler and binder phases. D: Coke with coarse ribbon mosaic texture and strongly anisotropic filler and binder phases. Observe large porosity (Po). E: Laminated, pore-lining anisotropic pyrolytic carbon. Insert is taken under cross-polars with a retarder plate. F: Laminated pyrolytic carbon with strong anisotropy. %CRo = coke reflectance.

in both sections. Because the initial organic matter was primarily Type II kerogen, the volatiles generated within the contact zone of the sills would be primarily methane (CH_4), and to a lesser extent, carbon dioxide (CO_2) (Tissot and Welte, 1984; Aarnes et al., 2011; Mahlstedt and Horsfield, 2012; Peters et al., 2005).

Several studies have evaluated the fate of the volatiles generated from organic-rich shales by igneous intrusions (e.g., Svensen et al., 2007; Aarnes et al., 2011; de Kock et al., 2017). Aarnes et al., 2011) observed that the buildup of pressure from petroleum generation by the intrusions caused large-scale emplacement-related fracturing of the host shales, most of which are rooted within the contact aureoles of the sills. These structures can serve as preferred pathways for the escape of volatile matter and heat to the atmosphere (Svensen et al., 2007; Aarnes et al., 2011; Senger et al., 2017) or as barriers to fluid flow depending on their network properties (Rabbel et al., 2021).

The isotopic composition of organic matter and petrographic observations suggest that a significant fraction of the volatiles was redeposited within the shales. ^{12}C is preferentially fractionated into volatiles and pyrolysates during organic matter cracking in the contact zone, increasing $\delta^{13}C$ values of the residual organic matter (Faure, 1986; Whiticar, 1996; Rimmer et al., 2005; Schimmelmann et al., 2009; Rahman et al., 2017). Thus, it is expected that the $\delta^{13}C$ values of the residual organic material would become less negative in values with decreasing distance to the sills. However, the trend of $\delta^{13}C$ values is a general shift towards more negative values approaching the aureoles, with a decrease of 3.13‰ over a distance of 8.7 m recorded towards the upper sill (Fig. 9A, Table 2).

An explanation for the isotopic trend observed within the aureoles is the trapping and redeposition of generated volatiles in form of pyrolytic carbon and associated organic alkylation reactions. Models of intrusion-sediment interactions recognize two stages (e.g., Podwysocki and Dutcher, 1971; Aarnes et al., 2011; Wang and Manga, 2015; Rabbel et al., 2021): An initial thermal phase, which is dominated by temperature-driven metamorphic reactions and fluid generation (resulting from the rapid generation of hydrocarbon and mineral dehydration), and a subsequent cooling phase dominated by fluid overpressure-driven shale fracturing and outward-directed fluid migration (Goodarzi et al., 2019; Rabbel et al., 2021). Thus, these models suggest a clear temporal sequence of fluid generation in a high-temperature environment followed by hydrofracturing and fluid migration in a cooler environment. However, the presence of vein-filling pyrolytic carbon with strong anisotropic texture (Figs. 11G, 12E-F) within the metamorphic aureoles suggests shale fracturing and fluid migration occurred at very high temperatures. Our observations tend to

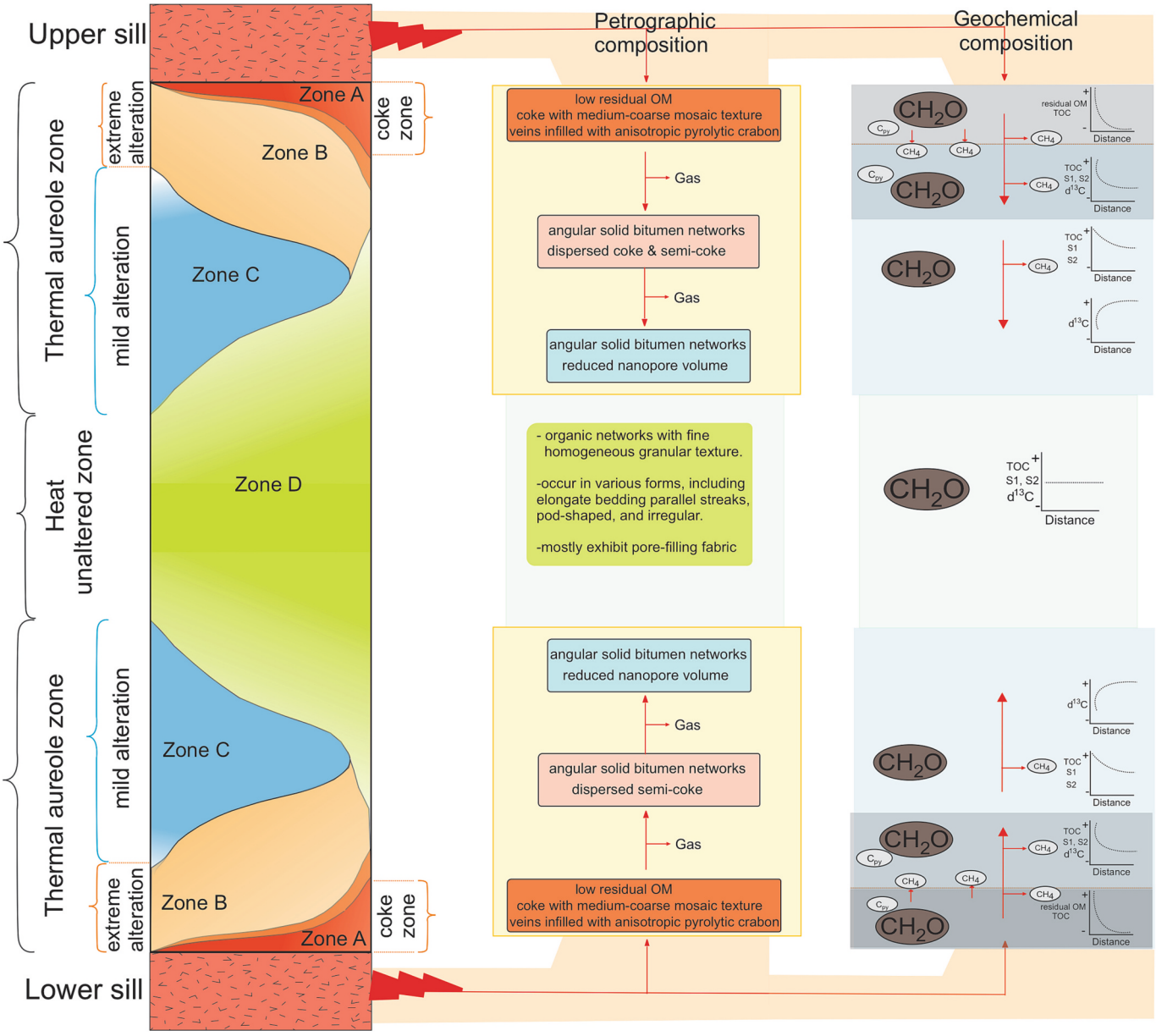

Fig. 12. Model interpretation of the effect of higher temperatures from sill emplacement on the petrographic and geochemical composition of organic matter in the Whitehill Formation. With decreasing distance to the sills, the optical texture of solid bitumen particles changed from isotropic to anisotropic and become progressively transformed into coke and pyrolytic carbon. These attributes allowed the aureole zone of the sills to be subdivided into an inner aureole zone with a notable presence of coke and pyrolytic carbon and an outer aureole zone with no coke and pyrolytic carbon. Within the inner contact zone of the upper sill, the optical texture and anisotropy of the coke and pyrolytic carbon also show distinctive changes with proximity to the sill. In approaching the sills, the isotopic composition of organic matter shows a progressive decrease (more negative values), which is interpreted to represent the migration of volatiles from the extremely altered shale layers adjacent to the sills and sequent cracking of both in-situ and migrated volatiles to pyrolytic carbon.

agree with the suggestion of Rabbel et al. (2021) that both the high-temperature chemical reactions and overpressure-driven fracturing and fluid migration occur almost simultaneously and that an immediate causal relationship exists between these processes. Thus, the flow of incipient hydrocarbon and other hydrothermal fluids from adjacent layers into aureoles likely occurred prior to significant cooling of the high-temperature environment, thereby allowing the methane to crack and become re-deposited in the form of pyrolytic carbon (Eq. (1); g = gas, s = solid) (Whiticar, 1996; Rimmer et al., 2005; Cooper et al., 2007; Schimmelmann et al., 2009; Rahman et al., 2017). It follows that the shales themselves may have served as a sink for generated volatiles in the form of pyrolytic carbon near the sill contacts:

$$CH4_{(g)} \rightarrow C_{(s)} + 2H_{2\ (g)} \quad (1)$$

With regard to alkylation reactions and isotopic exchange, Williams et al. (1988) have shown that alkylcyclohexanes and alkylbenzenes can be produced by such reactions in the presence of kerogen. The transfer of methyl groups from alkyldibenzothiophenes (4 positions, adjacent to the sulfur atom) to alkylaromatics in petroleum has also been demonstrated (Filley et al., 1997). Dissolved hydrocarbon gases may be involved in the alkylation process because the carbon in methane is isotopically very light, and alkylation would not need to be volumetrically extensive in order to bring about a lighter bulk isotopic composition. Some evidence for alkylation and isotope exchange has already been described (Sackett, 1993; Voigtmann et al., 1994), although the role played by alkylation, and the possible involvement of sulfur-species and macromolecular matrices will need further consideration (Fabuss et al., 1965; Williams

et al., 1988).

The development of anisotropic coke grains requires rapid exposure of oil-mature organic matter to a geological temperature of 350–450 °C, based on both experimental and field data (e.g., Taylor et al., 1998; Teichmuller and Teichmuller, 2002; Rimmer et al., 2005). Under laboratory conditions, a much higher temperature of up to 800 °C is required (e.g., Schimmelmann et al., 2009; Goodarzi et al., 2019). Although coke formation is partly governed by kinetics and could form at somewhat lower temperatures over longer periods (e.g., Banergie et al., 1986; Wang et al., 2022), the highly anisotropic texture of these coke grains suggests formation at high-temperature conditions.

Another piece of evidence for the generation of methane is the absence or sharp decrease in the abundance of organic material in the extremely altered strata immediately surrounding the sills. This observation indicates that the conversion of residual organic carbon to gaseous products operated effectively within the contact zone of the sills. This carbon-consuming reaction and generation of volatile products are promoted by supercritical H_2O-dominated fluids, which typically occur at elevated temperatures (Eq. (2); [s = solid, l = liquid, g = gas]) (Aarnes et al., 2011). Thus, these observations suggest that the organic matter in the contact zone of the sills attained the peak temperatures as predicted by thermal models (e.g., Teichmuller and Teichmuller, 2002; Aarnes et al., 2011; Wang and Manga, 2015):

$$2C_{(s)} + 2H_2O_{(l)} \rightarrow CH_{4\ (g)} + CO_{2\ (g)} \quad (2)$$

5.5. Impact of intrusions on the hydrocarbon system of the basin

Studies have shown that the high heat flow from igneous intrusions can affect all elements of both conventional and unconventional petroleum systems: source rock, reservoir, expulsion, migration pathways, seal, and the timely combination of all factors (e.g., Thomaz Filho et al., 2008; Aarnes et al., 2011; Goodarzi et al., 2019; Rabbel et al., 2021). In terms of the unconventional hydrocarbon system, igneous intrusions are generally considered unfavorable for resource potential as the organic matter in the contact zone has lost its capacity to generate hydrocarbon and the generated petroleum fluids have migrated out of the contact areas via emplacement-induced structures and fracture networks in the host shale and the intrusions. However, some studies (e.g., Spacapan et al., 2018; Goodarzi et al., 2019) contradict these general assumptions and present clear examples where gas content around sills is significantly higher than the background.

The results of petrographic and geochemical analyses presented here directly indicate that the high heat flow from the intrusions has destroyed the hydrocarbon generation potential in the highly metamorphosed aureole surrounding the sills. In particular, the decreased abundance of residual organic matter and its conversion to natural coke and pyrolytic carbon indicate that the organic matter in the contact zone of the sills has become metamorphosed and has lost its potential to generate hydrocarbons. Also, at the scale of the SEM, we document a reduced population of microporosity in the contact zone relative to the background (Fig. 7E, F). As methane adsorption capacity is typically associated with microporosity, this implies a reduced potential for adsorbed gas. Notwithstanding the loss of generation potential and reduced adsorption capacity in the contact zone, the effect of intrusions on the petroleum system of the organic-rich shale unit studied here is an overall positive one.

As organic maturation level is the main contributor to both shale porosity and permeability, the higher hydrocarbon generation potential of the sill-hosting section implies a higher potential for hydrocarbon storage and transmissibility. Also, the significant increase in mesoporosity in the contact zone, resulting from devolatilization pores in the coked shales, implies an increased storage capacity for free gas, which has been shown to be linked to the larger pores. Combined with the sealing capacity of the sills, these characteristics of the shales make their contact zone a good reservoir for free gas. The retention of free gas within the contact zone of the sill-hosting shales has been documented in several areas of the basin, but particularly in the study locality where this gas has been escaping from this shale unit where the equivalent of the upper sill was breached in a borehole at a depth of about 220 m for some 30 years (Macey et al., 2011). This gas has also been encountered recently in several water boreholes and windpumps at depth of 167 to 213 m in Loeriesfontein, and in some instances, the gas flow vigorously for several weeks. Thus, these observations indicate that igneous intrusions directly influence the distribution of meso- and microporosity in the reservoir shale and maybe be responsible for a significant variation of gas content on a basin-scale. Also, the variability of meso- and microporosity in the sill-hosting shales will also influence their capacity of other fluids, and by extension has significant implications for other geofluid systems, such as CO2 sequestration. However detailed understanding of these modifications and their implication for fluid storage requires a comprehensive understanding of the fracture network properties of the shales.

Additionally, the presence of vein-filling pyrolytic carbon in the aureole zone of the sills is an important discovery because it provides direct evidence for the formation of overpressure-induced hydraulic fractures and hydrocarbon fluid migration under high-temperature conditions. Although our thermal proxies are qualitative and cannot determine the exact temperature, the observed textural anisotropy of the pyrolytic carbon grains suggests that formation at temperatures of several hundred degrees. This observation is important because existing models of intrusion-sediment interactions tend to favor the idea that shale fracturing and fluid migration occur after the intrusion has cooled significantly and fluid pressure gradients have reversed from inward to outward-directed (e.g., Podwysocki and Dutcher, 1971; Aarnes et al., 2011; Wang and Manga, 2015; Rabbel et al., 2021). This observation has implications for the timing of fluid flow and migration pathways, including the role played by fracture networks in both the shales and the intrusions themselves as preferred pathways for fluid flow and/or barriers to flow (Rabbel et al., 2021).

6. Conclusions

This study evaluated the effects of igneous intrusions on the thermal evolution of oil-prone sedimentary organic matter and their implication for the development of shale resources in the Lower Permian Whitehill Formation, which is the principal reservoir shale in the Karoo Basin of South Africa. Results of organic petrographic and geochemical analyses indicate that organic matter in this shale formation is dominated by secondary hydrocarbons, comprising texturally homogenous, reflective pre-oil solid bitumen and nanoporous granular post-oil solid bitumen networks, which are derived from initial oil-prone sedimentary organic matter. Two sections are compared, one with two laterally continuous intrusive sills and a second without intrusions.

A comparison of the stratigraphic sections with and without sills indicates that the igneous intrusions, caused the TOC and S2 values to decline from a maximum of 17% to 10% and 62 mg HC/g TOC to 6.3 mg HC/g TOC. The reflectance of vitrinite and solid bitumen increased by a maximum of 1.26% to 6.13% and 3.03% to 7.95%, respectively. Results also indicate that the thermal aureole zone of the sills can be recognized by changes to the optical texture and morphology of the solid bitumen networks, as well as the isotopic composition of their constituent's micron-sized organic components. In approaching the sills, solid bitumen develops increasingly higher optical anisotropy and angularity, becomes increasingly converted into coke and pyrolytic carbon, and progressively depleted isotopically with $\delta^{13}C_{org}$ values becoming more negative by up to 3.13‰.

We also document that the aureole size of the two sills in the stratigraphic section of the shale examined is asymmetrical, with that of the upper aureole being 241% of the sill thickness while the lower aureole sill is 151%. Lithofacies variability, particularly differences in organic and clay mineral content of the intruded shale, may have caused its

thermal conductivity to vary and possibly accounts for this observation. The presence of highly anisotropic coke grains and pyrolytic carbon in the contact aureole of the sills is visual evidence for a substantial devolatilization of organic matter. Data also suggest that a fraction of gas that was generated was redeposited within the shales in the form of pyrolytic carbon. While elevated temperatures from the intrusions have destroyed petroleum generation and retention potential within the contact zone of the sills, the significant decrease of TOC and S2 values in the sill-bearing section relative to the background, suggests that intrusive heat may have improved methane generation. Moreover, our data indicate that overpressure-induced shale fracturing and hydrocarbon fluid migration can occur under high-temperature conditions, and prior to the cooling of the intrusions. This improved understanding of the role played by igneous intrusions in the generation and migration of methane will contribute to the search for and development of shale resources in the Karoo Basin and other similar basins.

Authors statement

This is a resubmission of COGEL-D-22-00534R1. We have addressed the concerns raised by Reviewer #2 as below.

Declaration of Competing Interest

The authors declare that they have no known competing financial interests or personal relationships that could have appeared to influence the work reported in this paper.

Data availability

Data will be made available on request.

Acknowledgments

This research was funded by the Upstream Training Trust of South Africa Karoo shale energy resource research grant. K.C. gratefully acknowledges Jenilee Steenkamp at Hantam Municipal Office in Loeriesfontein for brokering introduction to various farmers on whose properties the studied rock units are situated. The authors wish to express their grateful thanks to Prof Nicola Wagner at the University of Johannesburg for her assistance with organic petrographic analysis. We also appreciate reviews by Omid H. Ardakani and one anonymous that improved a previous version of this manuscript.

References

Aarnes, I., Svensen, H., Polteau, S., Planke, S., 2011. Contact metamorphic devolatilization of shales in the Karoo Basin, South Africa, and the effects of multiple sill intrusions. Chem. Geol. 281, 181–194.

Adeniyi, E.O., Ossa Ossa, F., Kramers, J.D., de Kock, M.O., Belyanin, G., Beukes, N.J., 2018. Cause and timing of the thermal over-maturation of hydrocarbon source rocks of the Ecca Group (Main Karoo Basin, South Africa). Mar. Pet. Geol. 91, 480–500. https://doi.org/10.1016/j.marpetgeo.2018.01.033.

Anderson, J.M., Schwyzer, F.V., 1977. The biostratigraphy of the Permian and Triassic. Part 4- Palaeomagnetic evidence for large-scale intra-Gondwana plate movements during the Carboniferous to Jurassic. Trans. Geol. Soc. S. Afr. 80, 211–234.

ASTM, 2014. Standard Test Method for Microscopical Determination of the Reflectance of Vitrinite Dispersed in Sedimentary Rocks. ASTM International, West Conshohocken, PA., USA, pp. D7708–D7714. www.astm.org.

Baker, L.L., Bernard, A., Rember, W.C., Milazzo, M., Dundas, C., Abramov, O., Keszthelyi, L., 2015. Temperature profile around a basaltic sill intruded into wet sediments. J. Volcanol. Geotherm. Res. 302, 81–86.

Banergie, D.K., Laidler, K.J., Nandi, B.N., Patmore, D.J., 1986. Kinetic studies of coke formation in hydrocarbon fraction of heavy crude. Fuel 65, 480–484.

Bernard, S., Horsfield, B., Schulz, H.-M., Wirth, R., Schreiber, A., 2012. Geochemical evolution of organic-rich shales with increasing maturity: a STXM and TEM study of the Posidonia Shale (Lower Toarcian, northern Germany). Mar. Pet. Geol. 31, 70–89.

Bohacs, K.M., Passey, Q.R., Rudnicki, M., Esch, W.L., Lazar, O.R., 2013. The spectrum of fine- grained reservoirs from 'shale gas' to 'shale oil'/tight liquids: essential attributes, key controls, practical characterization. In: International Petroleum Technology Conference. Beijing, China, March 26-28, 2013, Paper IPTC 16676. https://doi.org/10.2523/IPTC-16676-MS.

Cardott, B.J., Landis, C.R., Curtis, M.E., 2015. Post-oil solid bitumen network in the Woodford Shale, USA-a potential primary migration pathway. Int. J. Coal Geol. 139, 106–113.

Chukwuma, K., 2017. Spatial and Temporal Variations in the Geometry and Composition of the Permian Whitehill Formation, South Africa. PhD thesis,. University of Cape Town, p. 215. http://hdl.handle.net/11427/25057.

Chukwuma, K., Bordy, E.M., 2016. Spatiotemporal sedimentary facies variations in the Permian Whitehill Formation, main Karoo Basin. In: Linol, B., de Wit, M. (Eds.), Origin and Evolution of the Cape Mountains and Karoo Basin: Geo-biohistory in a terrain with shale gas resources and need for conservation, Part of the series Regional Geology Reviews 8643. Springer Verlag, pp. 101–110. https://doi.org/10.1007/978-3-319-40859-0-10.

Chukwuma, K., Bordy, E.M., Coetzer, A., 2018. Evolution of porosity and pore geometry in the Permian Whitehill Formation of South Africa-a FE-SEM image analysis study. Mar. Pet. Geol. 91, 262–278. https://doi.org/10.1016/j.marpetgeo.2017.12.026.

Chukwuma, K., Tsikos, H., Wagner, N., 2021. Control of variability of primary grain assemblages on the stratigraphic differences in diagenetic processes and products in organic-rich sediments. Sediment. Geol. 422, 105966 https://doi.org/10.1016/j.sedgeo.2021.105966.

Chukwuma, K., Tsikos, H., Wagner, N., Frazenburg, M., 2022. Dual sea-level-climatic controls on the stratigraphic distribution of total organic carbon content and macerals in the Permian black shales of Southwest Gondwana. J. Afr. Earth Sci. 188, 104495 https://doi.org/10.1016/j.jafrearsci.2022.104495.

Cole, D.I., McLachlan, I.R., 1991. Oil potential of the Permian Whitehill Shale Formation in the Main Karoo Basin, South Africa. In: Ulbrich, H., Rocha Campos, A.C. (Eds.), Proceedings and Papers of the Seventh Gondwana Symposium, Sao Paulo Instituto de Geosciences. Universidade de Sao Paulo, pp. 379–390.

Cole, D.I., McLachlan, I.R., 1994. Oil shale potential and depositional environment of the Permian Whitehill Shale Formation in the main Karoo Basin. In: Geological Survey of South Africa, 1994–0213, Open file report 1 &2, p. 145.

Cooper, J.R., Crelling, J.C., Rimmer, S.M., Whittington, A.G., 2007. Coal metamorphism by igneous intrusion in the Raton Basin, CO and NM: implications for generation of volatiles. Int. J. Coal Geol. 71, 15–27.

de Kock, M.O., Beukes, N.J., Adeniyi, E.O., Cole, D., Götz, A.E., Geel, C., Ossa, F.-G., 2017. Deflating the shale gas potential of South Africa's Main Karoo Basin. S. Afr. J. Sci. 113 https://doi.org/10.17159/sajs.2017/2016033, 2016–0331.

Desbois, G., Urai, J.L., Perez-Willard, F., Radi, Z., Offern, S., Burkart, I., Kukla, P.A., Wollenberg, U., 2013. Argon broad ion beam tomography in a cryogenic scanning electron microscope: a novel tool for the investigation of representative microstructures in sedimentary rocks containing pore fluid. J. Microsc. 249, 215–235.

Dong, T., Harris, N.B., 2020. The effect of thermal maturity on porosity development in the Upper Devonian-lower Mississippian Woodford Shale, Permian Basin, US: Insights into the role of silica nanospheres and microcrystalline quartz on porosity preservation. Int. J. Coal Geol. 217, 103346 https://doi.org/10.1016/j.coal.2019.103346.

Duncan, R., Hooper, P., Rehacek, J., Marsh, J., Duncan, A., 1997. The timing and duration of the Karoo igneous event, southern Gondwana. J. Geophys. Res. 102, 18127–18138.

Espitalié, J., Deroo, G., Marquis, F., 1985. Rock-Eval Pyrolysis and its Applications. Institut Français du Pétrole, Preprint no, p. 27299.

Fabuss, B.M., Duncan, D.A., Smith, J.O., Satterfield, C.N., 1965. Effect of organosulfurcompounds on the rate of thermal decomposition of selected saturated hydrocarbons. Ind. Eng. Chem. Proc. Design Dev. 4, 117–122.

Faure, G., 1986. Principles of Isotope Geology, second edition. John Wiley and Sons, New York, p. 589.

Faure, K., Cole, D.I., 1999. Geochemical evidence for lacustrine microbial blooms in the vast Permian main Karoo, Paraná, Falkland Islands and Huab basins of southwestern Gondwana. Palaeogeogr. Palaeoclimatol. Palaeoecol. 152, 189–213.

Filley, T.R., Filley, R.M., Eser, S., Freeman, K.H., 1997. Compound-specific isotope analyses of products from carbonization of a fluid catalytic cracking decant oil doped with 13C-enriched 4-methyldibenzothiophene. Energy Fuel 11, 637–646.

Geel, C., de Wit, M., Booth, P., Schulz, H.-M., Horsfield, B., 2015. Palaeo-environment, diagenesis and characteristics of Permian black shales in the lower Karoo Supergroup flanking the Cape Fold Belt near Jansenville, Eastern Cape, South Africa: implications for the shale gas potential of the Karoo Basin. S. Afr. J. Geol. 118, 248–274.

Goodarzi, F., Gentzis, T., Dewing, K., 2019. Influence of igneous intrusions on the thermal maturity of organic matter in the Sverdrup Basin, Arctic Canada. Int. J. Coal Geol. 213, 103280 https://doi.org/10.1016/j.coal.2019.103280.

Hackley, P.C., Zhang, T., Jubb, A.M., Valentine, B.J., Dulong, F.T., Hatcherian, J.J., 2020. Organic petrography of Leonardian (Wolfcamp A) mudrocks and carbonates, Midland Basin, Texas: the fate of oil-prone sedimentary organic matter in the oil window. Mar. Pet. Geol. 112, 104086 https://doi.org/10.1016/j.marpetgeo.2019.104086.

Hackley, P.C., Jubb, A.M., McAleer, R.J., Valentine, B.J., Birdwell, J.E., 2021. A review of spatially resolved techniques and applications of organic petrography in shale petroleum systems. Int. J. Coal Geol. 241, 103745.

Han, Y., Horsfield, B., Wirth, R., Mahlstedt, N., Bernard, S., 2017. Oil retention and porosity evolution in organic-rich shales. AAPG Bull. 101, 807–827. https://doi.org/10.1306/09221616069.

Hanson, R.B., Barton, M.D., 1989. Thermal development of low-pressure metamorphic belts- results from two-dimensional numerical-models. J. Geophys. Res. Solid Earth 94, 10363–10377.

Harris, N.B., Miskimins, J.L., Minch, C.A., 2011. Mechanical anisotropy in the Woodford Shale, Permian Basin: origin, magnitude, and scale. Lead. Edge 30, 284–291.

Harris, N.B., McMillan, J.M., Knapp, L.J., Mastalerz, M., 2018a. Organic matter accumulation in the Upper Devonian Duvernay Formation, Western Canada Sedimentary Basin, from sequence stratigraphic analysis and geochemical proxies. Sediment. Geol. 376, 185–203.
Harris, N.B., McMillan, J.M., Knapp, L.J., Mastalerz, M., 2018b. Organic matter accumulation in the Upper Devonian Duvernay Formation, Western Canada Sedimentary Basin, from sequence stratigraphic analysis and geochemical proxies. Sediment. Geol. 376, 185–203.
Horsfield, B., Zou, C., Li, J., Yang, S., Mahlstedt, N., Misch, D., Gross, D., Ma, W., Wang, Y., Tan, J., 2021. Prediction of the gas generating characteristics of the Qiongzhusi and Longmaxi Formations, Yangtze Platform, South China, using analogues. AAPG Bull. 105, 945–985. https://doi.org/10.1306/11182018244.
Jarvie, D.M., Hill, R.J., Ruble, T.E., Pollastro, R.M., 2007. Unconventional shale-gas systems: the Mississippian Barnett Shale of north-Central Texas as one model for thermogenic shale-gas assessment. AAPG Bull. 91, 475–499.
Johnson, M.R., Van Vuuren, C.J., Visser, J.N.J., Cole, D.I., DeV Wickens, H., Christie, A. D.M., Roberts, D.L., Brandl, G., Johnson, M.R., Anhaeusser, C.R., Thomas, R.J., 2006. Sedimentary rocks of the Karoo Supergroup. In: The Geology of South Africa: Geological Society of South Africa. Council for Geoscience.
Jourdan, F., Feraud, G., Bertrand, H., Watkeys, M., Kampunza, A., Le Gall, B., 2006. Basement control on dyke distribution in large igneous provinces: case study of the Karoo triple junction. Earth Planet. Sci. Lett. 241, 307–322.
Katz, B.J., Arango, I., 2018. Organic porosity: a geochemist's view of the current state of understanding. Org. Geochem. 123, 1–16.
Killops, S., Killops, V., 2005. Introduction to Organic Geochemistry, second edition. Blackwell Publishing, Malden, MA, USA, p. 406.
Könitzer, S.F., Leng, M.J., Davies, S.J., Stephenson, M.H., 2012. An assessment of geochemical preparation methods prior to organic carbon concentration and carbon isotope ratio analyses of fine-grained sedimentary rocks. Geochem. Geophys. Geosyst. 13, Q0AI02.
Liu, B., Mastalerz, M., Schieber, J., 2022. SEM petrography of dispersed organic matter in black shales: a review. Earth Sci. Rev. 224, 103874.
Loucks, R.G., Reed, R.M., Ruppel, S.C., Hammes, U., 2012. Spectrum of pore types and networks in mudrocks and a descriptive classification for matrix-related mudrock pores. AAPG Bull. 96, 1071–1098.
Macdonald, D., Gomez-Perez, I., Franzese, J., Spalletti, L., Lawver, L., Gahagan, L., Dalziel, I., Thomas, C., Trewin, N., Hole, M., Paton, D., 2003. Mesozoic break-up of SW Gondwana: implications for regional hydrocarbon potential of the southern South Atlantic. Mar. Pet. Geol. 20, 287–308.
Macey, P.H., Siegfried, H.P., Minaar, H., Almond, J., Botha, P.M.W., 2011. The Geology of Loeriesfontein Area- Explanation: Sheet 3018. Council for Geoscience, Pretoria, p. 344.
Mahlstedt, N., Horsfield, B., 2012. Metagenetic methane generation in gas shales I. Screening protocols using immature samples. Mar. Pet. Geol. 31, 27–42.
Mastalerz, M., Drobniak, A., Stankiewicz, A.B., 2018. Origin, properties, and implications of solid bitumen in source-rock reservoirs: a review. Int. J. Coal Geol. 195, 14–36.
Misch, D., Gross, D., Hawranek, G., Horsfield, B., Klaver, J., Mendez-Martin, F., Urai, J. L., Vranjes-Wessely, S., Sachsenhofer, R.F., Schmatz, J., Li, J., Zou, C., 2019. Solid bitumen in shales: petrographic characteristics and implications for reservoir characterization. Int. J. Coal Geol. 205, 14–31.
Nengovhela, V., Linol, B., Bezuidenhout, L., Dhansay, T., Muedi, T., de Wit, M., 2021. Shale gas leakage in lower Ecca shales during contact metamorphism by dolerite sill intrusions in the Karoo Basin, South Africa. S. Afr. J. Geol. 124, 443–464. https://doi.org/10.25131/sajg.124.0006.
Neumann, E.R., Svensen, H., Galerne, C.Y., Planke, S., 2011. Multistage evolution of dolerites in the Karoo large igneous province, Central South Africa. J. Petrol. 52, 959–984.
Nunn, J.A., Lin, G., 2002. Insulating effects of coals and organic shales: implications for topography-driven fluid-flow, heat-transport and genesis on ore deposits of the Arkoma Basin and Ozark Plateau. Basin Res. 14, 129–145.
Oelofsen, B.W., 1981. An Anatomical and Systematic Study of the Family Mesosauridae (Reptilia, Proganosauria) with Special Reference to its Associated Fauna and Palaeoecological Environment in the Whitehill Sea. Unpublished Ph.D. thesis,. University of Stellenbosch, p. 163.
Peters, K.E., Walters, C.C., Moldowan, J.M., 2005. The Biomarker Guide: Biomarkers and Isotopes in Petroleum Exploration and Earth History, second edition. Cambridge University Press, Cambridge, p. 700.
Podwysocki, M.H., Dutcher, R.R., 1971. Coal Dikes that intrude lamprophyre sills, Purgatoire River Valley, Colorado. Econ. Geol. 66, 267–280.
Rabbel, O., Palma, O., Mair, K., Galland, O., Spacapan, J.B., 2021. Fracture networks in shale- hosted igneous intrusions: Processes, distribution, and implication for igneous petroleum systems. J. Struct. Geol. 104403 https://doi.org/10.1016/j.jsg.2021.104403.
Radke, M., Welte, D.H., Willisch, H., 1986. Maturity parameters based on aromatic hydrocarbons: Influence of the organic matter. Org. Geochem. 10, 51–63.
Radke, M., Horsfield, B., Littke, R., Rullkötter, J., 1997. Maturation and petroleum generation. In: Welte, D.H., Horsfield, B., Baker, D.R. (Eds.), Petroleum and Basin Evolution, 169–230 Pp. Springer Verlag, Heidelberg.
Rahman, M.W., Rimmer, S.M., Rowe, H.D., Huggett, W.W., 2017. Carbon isotope analysis of whole-coal and vitrinite from intruded coals from the Illinois Basin: no isotopic evidence for thermogenic methane generation. Chem. Geol. 453, 1–11.
Raymond, A.C., Murchison, D.G., 1989. Organic maturation and its timing in a Carboniferous sequence in the Central Midland Valley of Scotland: comparisons with northern England. Fuel 68, 328–335.
Rimmer, S.M., Rowe, H.D., Hower, J.C., 2005. The effects of contact metamorphism on the elemental and isotopic composition of coal: An example from the Illinois Basin. In: 22nd Annual Meeting of the Society for Organic Petrologists-Abstracts.
Ross, D.J.K., Bustin, R.M., 2009. The importance of shale composition and pore structure upon gas storage potential of shale gas reservoirs. Mar. Pet. Geol. 26, 916–927.
Rowsell, D.M., De Swart, A.M.J., 1976. Diagenesis in Cape and Karroo sediments, South Africa, and its bearing on their hydrocarbon potential. Trans. Geol. Soc. S. A. 79, 81–145.
Sackett, W.M., 1993. Carbon isotope exchange between methane and amorphous carbon at 700°C. Org. Geochem. 20, 43–45.
Schimmelmann, A., Mastalerz, M., Gao, L., Sauer, P.E., Topalov, K., 2009. Dike intrusions into bituminous coal, Illinois Basin: H, C, N, O isotopic responses to rapid and brief heating. Geochim. Cosmochim. Acta 73, 6264–6281. https://doi.org/10.1016/j.gca.2009.07.027.
Senger, K., Millett, J., Planke, S., Ogata, K., Eide, C.H., Festoy, M., Galland, O., Jerram, D. A., 2017. Effects of igneous intrusions on the petroleum system: a review. First Break 35, 47–56.
Spacapan, J.B., Palma, J.O., Galland, O., Manceda, R., Rocha, E., D'Odorico, A., Leanza, H.A., 2018. Thermal impact of igneous sill complexes on organic-rich formations and implications for petroleum systems: a case study in the northern Neuquén Basin, Argentina. Mar. Pet. Geol. 91, 519–531.
Suárez-Ruiz, I., Flores, D., GracianoMendonça Filho, J., Hackley, P.C., 2012. Review and update of the applications of organic petrology: Part 1, geological applications. Int. J. Coal Geol. 99, 54–112.
Svensen, H., Planke, S., Chevallier, L., Malthe-Sorenssen, A., Corfu, F., Jamtveit, B., 2007. Hydrothermal venting of greenhouse gases triggering early Jurassic global warming. Earth Planet. Sci. Lett. 256, 554–566.
Taylor, G.H., Teichmüller, M., Davis, A., Diessel, C.F.K., Littke, R., Robert, P., 1998. Organic Petrology. Gebrüder Borntraeger, Berlin and Stuttgart, p. 704.
Teichmuller, M., Teichmuller, R., 2002. The chemical and structural metamorphosis of coal. Int. J. Earth Sci. 91, 75–99.
Teng, J., Liu, B., Mastalerz, M., Schieber, B., 2022. Origin of organic matter and organic pores in the overmature Ordovician-Silurian Wufeng-Longmaxi Shale of the Sichuan Basin, China. Int. J. Coal Geol. 253, 103970.
Thomaz Filho, A., Mizusaki, A.M.P., Antonioli, L., 2008. Magmatism and petroleum exploration in the Brazilian Paleozoic basins. Mar. Pet. Geol. 25, 143–151.
Tinker, J., de Wit, M., Brown, R., 2008. Mesozoic exhumation of the southern Cape, South Africa, quantified using apatite fission track thermochronology. Tectonophysics 455, 77–93.
Tissot, B.P., Welte, D.H., 1978. Petroleum Formation and Occurrence: A New Approach to Oil and Gas Exploration. Springer-Verlag, Heidelberg, New York, Berlin, p. 538.
Tissot, B.P., Welte, D.H., 1984. Petroleum Formation and Occurrence. Springer-Verlag, New York, p. 699.
Triguis, J.A., Arano, L.M., 1995. Parana Basin, Brasil: a huge pyrolyser. Comparison between molecular distributions in pyrolysed samples and source rocks affected by igneous intrusions. In: Grimalt, J.O., Dorronsoro, C. (Eds.), Organic Geochemistry: Developments and Applications to Energy, Climate, Environment, and Human History, pp. 512–514.
Van Krevelen, D.W., 1993. Coal Typology-Physics-Chemistry-Constitution, Third revised edition. Elsevier, p. 1002.
Vandenbroucke, M., Largeau, C., 2007. Kerogen origin, evolution and structure. Org. Geochem. 38, 719–833.
Visser, J.N.J., 1997. Deglaciation sequences in the Permo-Carboniferous Karoo and Kalahari Basins of southern Africa: a tool in the analysis of cyclic glaciomarine basin fills. Sedimentology 44, 507–521.
Voigtmann, M.F., Yang, K., Batts, B.D., Smith, J.W., 1994. Evidence for synthetic generation of methylphenanthrenes in sediments. Fuel 73, 1899–1903.
Wang, D., Manga, M., 2015. Organic matter maturation in the contact aureole of an igneous sill as a tracer of hydrothermal convection. J. Geophys. Res. 120, 4102–4112.
Wang, Y., Zhou, Y., Fan, S., Lang, X., Li, G., 2022. Influence of low-temperature oxidation of heavy oil coking by thermal pyrolysis during in situ combustion process. Fuel 316, 123314. https://doi.org/10.1016/j.fuel.2022.123314.
Whiticar, M.J., 1996. Stable isotope geochemistry of coals, humic kerogens, and related natural gases. Int. J. Coal Geol. 32, 191–215.
Williams, J.A., Dolcater, D.L., Torkelson, B.E., Winters, J.C., 1988. Anomalous concentrations of specific alkylaromatic and alkylcycloparaffin components in West Texas and Michigan crude oils. Org. Geochem. 13, 47–59.
Yang, S., Horsfield, B., 2016. Some predicted effects of minerals on the generation of petroleum in nature. Energy Fuel 30, 6677–6687.